8-2011

A Priori Analysis of Subgrid-Scale Pressure in High Pressure H_2/O_2 Mixing and Reacting Shear Layers

Zhiyuan Ma
Clemson University, zhiyuam@clemson.edu

A PRIORI ANALYSIS OF SUBGRID-SCALE PRESSURE IN HIGH PRESSURE H_2/O_2 MIXING AND REACTING SHEAR LAYERS

A Thesis
Presented to
the Graduate School of
Clemson University

In Partial Fulfillment
of the Requirements for the Degree
Master of Science
Mechanical Engineering

---

by
Zhiyuan Ma
August 2011

Accepted by:
Dr. Richard S. Miller, Committee Chair
Dr. Donald E. Beasley
Dr. Rui Qiao

Abstract

An *a priori* analysis of subgrid-scale pressure in high pressure combustion is carried out using three different flow fields obtained by direct numerical simulation (DNS). The simulations directly solve the Navier-Stokes equations of high pressure, transitional H_2/O_2 mixing and reacting shear layers employing a cubic Peng-Robinson real gas state equation. Detailed chemistry, multicomponent, differential, and cross diffusion are included. The results are analyzed to provide subgrid information relevant to Large Eddy Simulation (LES) of turbulent combustion. The analysis includes a detailed comparison of the actual filtered pressure with its corresponding form evaluated with the filtered primitive variables. Although negligible for purely mixing cases, the gradient of the subgrid pressure is shown to be of the same order, or larger than, the corresponding divergence of the turbulent subgrid stresses for reacting cases. This is despite the fact that all species behave essentially as ideal gases for this flame. The analysis is conducted through both a global perspective, as well as by conditioning on specific regions of the flame; including regions of large subgrid kinetic energy, large subgrid scalar dissipation, large temperature, etc., in order to isolate its effect within certain regions of the flame. The results indicate that subgrid pressure modeling can be important for accurate LES. A dynamic similarity model for the subgrid pressure is therefore introduced and shows substantial improvement in predicting the filtered pressure for reacting flows. However, its improvement is diminished when considering

the pressure gradient.

Acknowledgments

A very special thanks goes out to Dr. Miller, without whose motivation and encouragement I would not have finshed my Master's degree and considered further research in turbulent combustion. His expertise and patience are much appreciated. He devoted great effort to my graduate study that established and expanded my understanding of turbulent flow.

I must acknowledge Justin Forster, who gave me lots of helpful suggestion both in coding and writing this thesis.

I would also like to thank Dr. Beasley and Dr. Qiao for not only being on my committee, but also for offering valuable advice for this work.

Finally, I would like to dedicate this thesis to my parents, who motivated my interest in engineering and supported me my entire life.

Table of Contents

List of Tables

List of Figures

Chapter 1

Introduction

Because of ongoing advances in computational ability, numerical simulation has played an increasingly significant role in analyzing reacting flows; especially under supercritical conditions too costly and complex to be widely studied using experimental methods. Direct numerical simulation (DNS), an example of one such numerical simulation, directly solves all spatial and temporal scales of a flow providing the most accurate flow field information currently available. Much research effort has been focused on using this method to study both non-reacting [36, 54, 26] and reacting flows [62, 15, 53, 34, 37]. However, while DNS is acurate, it requires extensive computational time and resources. To capture the turbulent motions in all scales, the grid size and time step scale in order of $Re^{-9/4}$ and $Re^{-3/2}$, respectively. Meaning, even to calculate a small region with a Reynold's number less than 10^3, millions of grid points are needed and the code can run for long time. As a result, DNS is typically used only to simulate a small region in specific research flows.

To simulate practical flows, which are accompanied by high Reynold's numbers and complex geometry, Reynolds Averaged Navier-Stokes (RANS) and Large Eddy Simulation (LES) are the methods most frequently used. RANS can save much

computational effort by calculating only the mean flow field, with effects of the fluctuations being estimated using various model. However, one of RANS's weakest areas is turbulent combustion is due to the highly non-linear nature of chemical reaction rates. In contrast, LES is a relatively less used method that has received much academic attention since the early 1990s [8, 30, 23, 35, 17, 57, 60, 61]. Compared with RANS, LES can predict scalar dissipation rates more accurately [45, 44, 50], which consequently result in a more accurate chemical reaction rate estimation. As a result LES is generally considered as a more promising pratical method than DNS and RANS.

In LES, each instantaneous variable is decomposed into a "resolved" scale plus a subgrid scale fluctuating component, mathematicaly represented by, $\Phi = \bar{\Phi} + \Phi'$. The filtered variable, $\bar{\Phi}$, is mathematically defined in Eq. (1.1):

$$\bar{\Phi}(x) = \int_{\Omega} \Phi(x_j^{'}) G(x_j - x_j^{'}) dx_j^{'} \tag{1.1}$$

where $G(x_j)$ represents the filter kernel defined over the domain, Ω. Similar to a PDF, $G(x_j)$ must integrate to unity. The most common form is a spatially local "box" filter. Compressible flows use the concept of Favre filtering, which is a density-weighted filter related to the standard filter represented by the expression, $\tilde{\Phi} = \overline{\rho\Phi}/\bar{\rho}$. Then the variables can be decomposed by Favre filtering, mathematically represented as $\Phi = \tilde{\Phi} + \Phi''$.

The full compressible Navier-Stokes governing equations are:

$$\frac{\partial \rho}{\partial t} + \frac{\partial}{\partial x_j}[\rho u_j] = 0 \tag{1.2}$$

$$\frac{\partial}{\partial t}\rho u_i + \frac{\partial}{\partial x_j}[\rho u_i u_j + P\delta_{ij} - \tau_{ij}] = 0 \tag{1.3}$$

$$\frac{\partial}{\partial t}\rho e_t + \frac{\partial}{\partial x_j}[(\rho e_t + P)u_j - u_i\tau_{ij} + Q_{BK_j} + \sum_{\alpha=1}^{N} H_{,\alpha}J_{j,\alpha}] = S_e \tag{1.4}$$

$$\frac{\partial}{\partial t}\rho Y_\alpha + \frac{\partial}{\partial x_j}[\rho Y_\alpha u_j + J_{j,\alpha}] = S_{Y_\alpha} \tag{1.5}$$

where subscript i and j are vectors in physical space, t the time, x_j the spatial coordinate vector, ρ the mixture density, P the pressure, e_t the total energy, δ_{ij} the Kronecker delta tensor, τ_{ij} the (Newtonian) viscous stress tensor, Q_{BK_j} the Bearman-Kirkwood form of the heat flux vector, $J_{j,\alpha}$ the mass flux vector for species α, $\sum_{\alpha=1}^{N} H_{,\alpha}J_{j,\alpha}$ the enthalpy flux (N being the total number of species), S the chemical reaction source term, Y_α the mass fraction for specie α. By filtering these equations, the LES governing equations are:

$$\frac{\partial \bar{\rho}}{\partial t} + \frac{\partial \bar{\rho}\widetilde{u_j}}{\partial x_j} = 0 \tag{1.6}$$

$$\frac{\partial \bar{\rho}\widetilde{u_i}}{\partial t} + \frac{\partial \bar{\rho}\widetilde{u_i}\widetilde{u_j}}{\partial x_j} = -\frac{\partial P(\bar{\Psi})}{\partial x_i} + \frac{\partial \tau_{ij}(\bar{\Psi})}{\partial x_j} - \frac{\partial}{\partial x_i}[\overline{P(\Psi)} - P(\bar{\Psi})] + \frac{\partial}{\partial x_j}[\overline{\tau_{ij}} - \tau_{ij}(\bar{\Psi})] - \frac{\partial \Pi_{ij}}{\partial x_j} \tag{1.7}$$

$$\frac{\partial \bar{\rho}\widetilde{e_t}}{\partial t} + \frac{\partial \bar{\rho}\widetilde{e_t}\widetilde{u_j}}{\partial x_j} = -\frac{\partial P(\bar{\Psi})\widetilde{u_j}}{\partial x_j} + \frac{\partial \widetilde{u_i}\tau_{ij}(\bar{\Psi})}{\partial x_j} - \frac{\partial Q_{BK_j}(\bar{\Psi})}{\partial x_j} + \frac{\partial}{\partial x_j}[\sum_{\alpha=1}^{N}\overline{H_{,\alpha}J_{j,\alpha}}] + \overline{S_e} \tag{1.8}$$

$$- \frac{\partial}{\partial x_j}[\overline{Q_{BK_j}} - Q_{BK_j}(\bar{\Psi})] + \frac{\partial}{\partial x_j}[\overline{u_i\tau_{ij}} - \widetilde{u_i}\tau_{ij}(\bar{\Psi})] \tag{1.9}$$

$$- \frac{\partial}{\partial x_j}[\bar{\rho}\widetilde{e_t}\widetilde{u_j} - \bar{\rho}\widetilde{e_t}\widetilde{u_j}] - \frac{\partial}{\partial x_j}[\overline{P(\Psi)} - P(\bar{\Psi})]\widetilde{u_j} \tag{1.10}$$

$$\frac{\partial \bar{\rho}\widetilde{Y_\alpha}}{\partial t} + \frac{\partial \bar{\rho}\widetilde{Y_\alpha}\widetilde{u_j}}{\partial x_j} = -\frac{\partial J_{j,\alpha}(\bar{\Psi})}{\partial x_j} + \overline{S_{Y_\alpha}} - \frac{\partial}{\partial x_j}[\bar{\rho}\widetilde{Y_\alpha u_j} - \bar{\rho}\widetilde{Y_\alpha}\widetilde{u_j}] - \frac{\partial}{\partial x_j}[\overline{J_{j,\alpha}} - J_{j,\alpha}(\bar{\Psi})] \tag{1.11}$$

where $\overline{P(\Psi)}$ the filtered pressure, which is calculated by directly filtering pressure; The resolved pressure $P(\bar{\Psi})$ is calculated by the filtered primitive variables; The subgrid turbulent stress Π_{ij} is calculated by $\Pi_{ij} = \bar{\rho}(\widetilde{u_i u_j} - \widetilde{u_i}\widetilde{u_j})$. Noted that, we specify Ψ to represent the primitive variables (*eg.* density ρ, velocity vector u_i, energy

e_t, and mass fraction Y_α). In contrast,$\bar{\Psi}$ represents the set of appropriatedly filtered primitive variables (*eg.* $\bar{\rho}$, $\widetilde{u_i}$, $\widetilde{e_t}$, $\widetilde{Y_\alpha}$), while $\Phi(\bar{\Psi})$ represents a variable calculated from the filtered primitive variables (*eg.* $P(\bar{\Psi})$, $T(\bar{\Psi})$).

Equations (1.6) - (1.11) yield several unclosed terms, including the subgrid turbulent stress divergence $\frac{\partial \Pi_{ij}}{\partial x_j}$, subgrid viscous term $\frac{\partial}{\partial x_j}[\overline{\tau_{ij}} - \tau_{ij}(\bar{\Psi})]$, subgrid pressure dilatation $\frac{\partial}{\partial x_j}[\overline{P(\Psi)} - P(\bar{\Psi})]\widetilde{u_j}$, the filtered chemical reaction source term $\widetilde{S}$, subgrid heat flux $\frac{\partial}{\partial x_j}[\overline{Q_{BK_j}} - Q_{BK_j}(\bar{\Psi})]$, subgrid convective energy $\frac{\partial}{\partial x_j}[\bar{\rho}\widetilde{e_t u_j} - \bar{\rho}\widetilde{e_t}\widetilde{u_j}]$, subgrid viscous energy $\frac{\partial}{\partial x_j}[\widetilde{u_i \tau_{ij}} - \widetilde{u_i}\tau_{ij}(\bar{\Psi})]$, and subgrid mass flux $\frac{\partial}{\partial x_j}[\overline{J_{j,\alpha}} - J_{j,\alpha}(\bar{\Psi})]$, that may require modeling as they contain unresolved information about the subgrid scales. Of these unclosed terms, the filtered chemical reaction rate, $\widetilde{S_{Y_\alpha}}$, and subgrid turbulent stresses, Π_{ij}, have received the most attention. The most frequently used methods to model the chemical reaction term are the Laminar Flamelet and Probability Density Function methods, both of which have been found to predict the chemical reaction rate reasonably accurately for near equilibrium flames [40, 48, 47, 49, 4]. For other subgrid terms, the dynamic/similarity method is often used [14, 6, 43, 56, 31, 2, 5, 20].

In addition to these unclosed terms, the filtered pressure, $\overline{P(\Psi)}$, may also be an unknown term depending on the formulation, because it requires the value of the instanstaneous primitive variables, Ψ, which LES cannot provide. One exception is the single species ideal gas law for which $\overline{P(\Psi)} = \bar{\rho}R\tilde{T}$, [*eg.* $\overline{P(\Psi)} = P(\tilde{\Psi})$], where R is the universal gas constant. Few previous studies regarding the filtered pressure in the momentum equation exist; most of them simply assume it equals the resolved pressure, $P(\bar{\Psi})$, and thus their difference $[\overline{P(\Psi)} - P(\tilde{\Psi})]$ is neglected with no clear justification. However, the subgrid pressure may have a significant effect on the combustion process due to its multicomponent nature [18, 32, 24, 29, 27, 28, 19].

For ideal gas mixtures:

$$P = \rho(\sum_{\alpha=1} Y_\alpha/M_\alpha)RT, \tag{1.12}$$

where M_α is the molecular weight of species α, and the summation is over all species. When filtering Eq. (1.12), the term $\sum_{\alpha=1}^{N} Y_\alpha/M_\alpha$ can no longer be removed from the filtering operation. Therefore, the above assumption may not hold. In this case:

$$\overline{P(\Psi)} = \bar{\rho}(\sum_{\alpha=1}^{N} \frac{\widetilde{Y_\alpha}}{M_\alpha})R\tilde{T} + P_{sgs} \tag{1.13}$$

where P_{sgs} is defined as the difference between $\overline{P(\Psi)}$ and $P(\bar{\Psi})$ $\left(P(\bar{\Psi}) = \bar{\rho}(\sum_{\alpha=1}^{N} \frac{\widetilde{Y_\alpha}}{M_\alpha})R\tilde{T}\right)$.

In high pressure compressible flows, subgrid pressure effects may be even stronger due to the use of real gas state equations [11]. This is because real gas state equations for mixtures are often complex and may be highly nonlinear. For this work, the Peng-Robinson (PR) equation of state (EOS) is used:

$$P(\Psi) = \frac{RT}{v - B_m} - \frac{A_m}{v^2 + 2vB_m - B_m^2}, \tag{1.14}$$

$$v = \frac{\sum_\alpha X_\alpha M_\alpha}{\rho}, \tag{1.15}$$

$$X_\alpha = \frac{Y_\alpha/M_\alpha}{(\sum_{\alpha=1} \frac{Y_\alpha}{M_\alpha})}, \tag{1.16}$$

where v is the specific mole volume, X_α the species mole fraction; and the temperature is T. The temperature is calculated by an iterative Newton-Raphson scheme [10], as it is represented by an implicit function of the density, species mass fractions, and internal energy $[T = f(\rho, Y_\alpha, (e_t - \frac{1}{2}u_i u_i)]$. The mixture parameters A_m and B_m are

calclulated by the following mixing rules [16, 33]:

$$A_m = \sum_\alpha \sum_\beta X_\alpha X_\beta A_{\alpha\beta}, \tag{1.17}$$

$$B_m = \sum_\alpha X_\alpha B_\alpha, \tag{1.18}$$

$$A_{\alpha\beta} = 0.457236(\overline{R}T^c_{\alpha\beta})^2 \left[1 + C_{\alpha\beta}\left(1 - \sqrt{T/T^c_{\alpha\beta}}\right)\right]^2 / P^c_{\alpha\beta} \ , \tag{1.19}$$

$$B_\alpha = 0.077796 \ \overline{R}T^c_{\alpha\alpha}/P^c_{\alpha\alpha} \ , \tag{1.20}$$

$$C_{\alpha\beta} = 0.37464 + 1.54226\Omega_{\alpha\beta} - 0.26992\Omega^2_{\alpha\beta} \ , \tag{1.21}$$

where the superscript c indicates critical properties. The diagonal elements of the critical matrices are equal to their pure substance counterparts; *eg.* $T^c_{\alpha\alpha} = T^c_\alpha$, $P^c_{\alpha\alpha} = P^c_\alpha$, and $\Omega_{\alpha\alpha} = \Omega_\alpha$, where Ω_α is the acentric factor of species α. The off-diagonal elements are evaluated as follows:

$$T^c_{\alpha\beta} = \sqrt{T^c_{\alpha\alpha}T^c_{\beta\beta}}(1 - k_{\alpha\beta}), \qquad P^c_{\alpha\beta} = Z^c_{\alpha\beta}(\overline{R}T^c_{\alpha\beta}/\overline{v}^c_{\alpha\beta}), \tag{1.22}$$

$$\overline{v}^c_{\alpha\beta} = \frac{1}{8}\left[\left(\overline{v}^c_{\alpha\alpha}\right)^{1/3} + \left(\overline{v}^c_{\beta\beta}\right)^{1/3}\right]^3, \qquad Z^c_{\alpha\beta} = \frac{1}{2}\left(Z^c_{\alpha\alpha} + Z^c_{\beta\beta}\right), \qquad \Omega_{\alpha\beta} = \frac{1}{2}\left(\Omega_{\alpha\alpha} + \Omega_{\beta\beta}\right), \tag{1.23}$$

where the diagonal elements of each of the above symmetric matrices are also equal to the pure substance values. The binary interaction parameter, $k_{\alpha\beta}$, is a function of the species being considered and is taken to be $k_{\alpha\beta} = 0.1$ for $\alpha \neq \beta$ and $k_{\alpha\alpha} = 0$.

Then the filtered pressure, $\overline{P(\Psi)}$, is calculated by directly filtering Eq. (1.14) as:

$$\overline{P(\Psi)} = \overline{\frac{RT}{v - B_m} - \frac{A_m}{v^2 + 2vB_m - B_m^2}}, \tag{1.24}$$

and the resolved pressure, $P(\bar{\Psi})$, is calculated by the "resolved" primitive variable as:

$$P(\bar{\Psi}) = \frac{RT(\bar{\Psi})}{v(\bar{\Psi}) - B_m(\bar{\Psi})} - \frac{A_m(\bar{\Psi})}{v(\bar{\Psi})^2 + 2v(\bar{\Psi})B_m(\bar{\Psi}) - B_m(\bar{\Psi})^2} \ , \tag{1.25}$$

$$v(\bar{\Psi}) = \frac{\sum_\alpha X_\alpha(\bar{\Psi})M_\alpha}{\bar{\rho}} \ , \tag{1.26}$$

$$X_\alpha(\bar{\Psi}) = \frac{\widetilde{Y_\alpha}}{M_\alpha(\sum_{\alpha=1} \frac{\widetilde{Y_\alpha}}{M_\alpha})} \ , \tag{1.27}$$

$$A_m(\bar{\Psi}) = \sum_\alpha \sum_\beta X_\alpha(\bar{\Psi})X_\beta(\bar{\Psi})A_{\alpha\beta} \ , \tag{1.28}$$

$$B_m(\bar{\Psi}) = \sum_\alpha X_\alpha B_\alpha \ , \tag{1.29}$$

where $T(\bar{\Psi})$ is the "resolved" temperature calculated from Favre filtered internal energy and species mass fracction [*i.e.* $T(\bar{\Psi}) = f(\widetilde{Y_\alpha},\ \widetilde{e_t} - \frac{1}{2}\widetilde{u_i}\widetilde{u_i})$], $v(\bar{\Psi})$ the "resolved" specific mole volume, $X_\alpha(\bar{\Psi})$ the "resolved" mole fraction, $A_m(\bar{\Psi})$ and $B_m(\bar{\Psi})$ the "resolved" mixture parameters.

Therefore, in high pressure compressible reacting flows, the filtered pressure calculted from Eq. (1.24) could be significantly different from the resolved pressure evaluated from Eq. (1.25). As a result, it is not suitable to assume simply that the resolved pressure is equal to the filtered pressure. To further quantify the difference between the filtered pressure and resolved pressure, this work divides the filtered pressure into two terms; the resolved pressure, $P(\bar{\Psi})$, and the subgrid pressure, $P_{sgs} = \overline{P(\Psi)} - P(\bar{\Psi})$:

$$\overline{P(\Psi)} = P(\bar{\Psi}) + P_{sgs}. \tag{1.30}$$

Furthermore, even if the subgrid pressure is small enough to be neglected, the filtered pressure gradient $[\partial\overline{P(\Psi)}/\partial x_i]$ may be different from the resolved pressure gradient $[\partial P(\bar{\Psi})/\partial x_i]$. It is the gradient of P_{sgs} that directly appears in the LES momentum

equation [Eq. (1.7)]. Derivatives enhance small length scale features being proportional to the wave number in the spectral domain. As P_{sgs} is a small scale quantity, its relative gradient is expected to be amplified. Selle *et al.* [58] also empoyed the Peng-Robinson state equation for high pressure DNS. They have demonstrated the significance of this term in a supercritical binary mixing flow, and developed a model based on the Taylor series expansion of the EOS. The model results were accurate for small filter widths, but its performance decreased as the filter width increased. They also stated that the model is too complex for application in an actual LES. No other investigation of the subgrid pressure for real gas equations of state, in either mixing or reacting flows, are known to the authors.

The primary objective of the present work is to conduct *a priori* analyses of the filtered pressure, the subgrid pressure, and associated primitive variables, both in the mixing flow and reacting flows based on the DNS data provided by Foster and Miller [10, 12]. Based on the *a priori* analyses, a subgrid pressure model is also proposed.

Chapter 2

DNS database and approach

The specific interest of this work is the relative effect of the subgrid pressure in LES of turbulent reacting flows. As an example flow field, a previously computed DNS database for a temporally developing reacting shear layer is considered [12]. The DNS governing equations used here include real gas effects, detailed chemistry, and multicomponent, differential, and cross diffusion [10, 12]. The chemical reaction is calculated by a detailed 19-step, 8 species (H_2, O_2, H_2O, OH, H, O, HO_2, and H_2O_2) chemical mechanism by Sohn *et al.* [59], shown in Table 2.1.

As shown in Fig. 2.1, the computational domain is a non-premixed hydrogen-oxygen temporally developing shear layer, with the oxygen stream at the top and hydrogen stream at the bottom, flowing in opposite directions. The initial vorticity thickness, $\delta_{\omega 0}$, is calculated by $\delta_{\omega 0} = |\frac{\Delta U_0}{<\partial u_1/\partial x_2>_{max}}|$, where the brackets indicate averaging over homogeneous x_1 - x_3 planes, and ΔU_0 is the velocity difference across the two streams $\Delta U_0 = \frac{U_1 - U_2}{2}$. The different initial conditions used for the *a priori* analysis are summarized in Table 2, where Δ_1 is the uniform grid spacing in the x_1 direction, N_i the number of grid points in i direction, $M_{c,0}$ the initial convective Mach number, Re_0 the initial Reynolds number defined as $Re_0 = \Delta U_0 \delta_{\omega 0} \rho_0 / \mu_0$, where ρ_0

ID	***Reaction***	$A[cm.mole.s]$	β	$E_a[kJ/mole]$
1	$O_2 + H \rightleftharpoons OH + O$	2.00×10^{14}	0.00	70.30
2	$H_2 + O \rightleftharpoons OH + H$	5.06×10^{4}	2.67	26.30
3	$H_2 + OH \rightleftharpoons H_2O + H$	1.00×10^{8}	1.60	13.8
4	$OH + OH \rightleftharpoons H_2O + O$	1.50×10^{9}	1.14	0.42
5	$H + H + M \rightleftharpoons H_2 + M$	1.80×10^{18}	-1.00	0.00
6	$H + OH + M \rightleftharpoons H_2O + M$	2.20×10^{22}	-2.00	0.00
7	$O + O + M \rightleftharpoons O_2 + M$	2.90×10^{17}	-1.00	0.00
8	$H + O_2 + M \rightleftharpoons HO_2 + M$	2.30×10^{18}	-0.80	0.00
	k_∞	4.52×10^{13}	0.00	0.00
9	$HO_2 + H \rightleftharpoons OH + OH$	1.50×10^{14}	0.00	4.20
10	$HO_2 + H \rightleftharpoons H_2 + O_2$	2.50×10^{13}	0.00	2.90
11	$HO_2 + H \rightleftharpoons H_2O + O$	3.00×10^{13}	0.00	7.20
12	$HO_2 + O \rightleftharpoons OH + O_2$	1.80×10^{13}	0.00	-1.70
13	$HO_2 + OH \rightleftharpoons H_2O + O_2$	6.00×10^{13}	0.00	0.00
14	$HO_2 + HO_2 \rightleftharpoons H_2O_2 + O_2$	2.50×10^{11}	0.00	-5.20
15	$OH + OH + M \rightleftharpoons H_2O_2 + M$	3.25×10^{22}	-2.00	0.00
	k_∞	7.45×10^{13}	-0.37	0.00
16	$H_2O_2 + H \rightleftharpoons H_2 + HO_2$	1.70×10^{12}	0.00	15.70
17	$H_2O_2 + H \rightleftharpoons H_2O + OH$	1.00×10^{13}	0.00	15.00
18	$H_2O_2 + O \rightleftharpoons OH + HO_2$	2.80×10^{13}	0.00	26.80
19	$H_2O_2 + OH \rightleftharpoons H_2O + HO_2$	5.40×10^{12}	0.00	4.20

Table 2.1: Detailed chemical kinetic mechanism for H_2/O_2 combustion [59] and corresponding forward reaction constants: $k_r = AT^{\beta}exp(-E_A/\overline{R}T)$. Third body efficiencies: $H_2 = 1.00$, $O_2 = 0.35$, $H_2O = 6.5$. Reaction rate coefficients dependent on pressure are calculated as $k_r = k_\infty k_0[M]/(k_\infty + k_0[M])$ where k_0, and k_∞ are the low and high pressure reaction rate coefficients, respectively.

and μ_0 are the average density and viscosity of each free stream value, respectively. The procedure for solving these equations can be found in Foster and Miller [10, 39]. In summary, the time derivatives are solved by a fourth order Runge-Kutta integration routine and the spatial derivatives are solved by an eighth order central explicit finite difference method. Tenth order filtering is also applied at each Runge-Kutta stage to reduce spurious oscillations in the solution. Parallelization is achieved by incorporating the Message Passing Interface (MPI) routines to decompose the computational domain in all three directions. Simulations were conducted on Clemson University's "Palmetto Cluster," and the simulations used up to 2,016 processing cores each. Both reacting and purely mixing simulations are considered at Reynolds numbers ranging from 850 - 2500. Simulation parameters are provided in Table 2

A spherical top-hat filter is applied to the DNS data to provide both the resolved LES field as well as the subgrid information which would be unavailable in an actual LES. It can be mathematically represented by:

$$\widetilde{G}(x_j - x_j^{'}) = \begin{cases} \frac{1}{\pi\Delta^3/6} & |x_j - x_j^{'}| \leq \Delta/2 \\ 0 & |x_j - x_j^{'}| > \Delta/2 \end{cases} \tag{2.1}$$

The filtered pressure, $\overline{P(\Psi)}$, is evaluated by directly filtering the actual DNS pressure; while the resolved pressure, $P_r = P(\bar{\Psi})$, is calcutated by Eqs. (1.25) - (1.29) as a function of the appropriately filtered primitive variables; and the subgrid pressure is calculated by $P_{sgs} = \overline{P(\Psi)} - P_r = P(\bar{\Psi})$. It is reasonable to assume that large unclosed terms in the filtered DNS data may require modeling [58, 21, 9, 3] in an actual LES. To investigate the effects of the filter width on the subgrid scales, the filter width, Δ, used in this analysis is $5\Delta_1$, $11\Delta_1$, and $25\Delta_1$, respectively, where Δ_1 is the uniform DNS grid size in the x_1 direction. The corresponding filter widths nondimensionized

by the initial vorticity thickness ($\delta_{\omega 0}$) are $\Delta/\delta_{\omega 0} \approx 0.6$, $\Delta/\delta_{\omega 0} \approx 1.2$, and $\Delta/\delta_{\omega 0} \approx 3.0$, repectively.

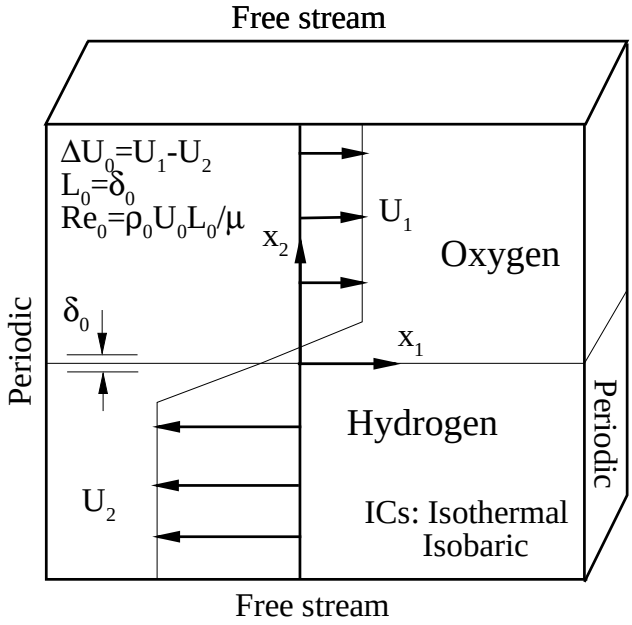

Figure 2.1: Computational domain.

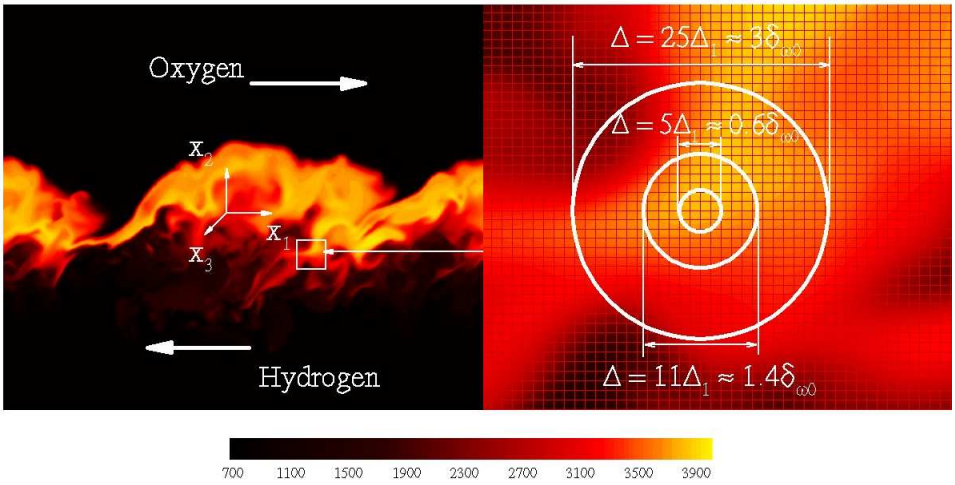

Figure 2.2: Instantaous centerline countours of the temperature distribution in [K] at $t^* = 115$, for the $Re_0 = 2500$ reacting flow DNS, and relative filter widths.

	MIX1	***REACT***1	***REACT***2
Species1	O_2	O_2	O_2
Species2	H_2	H_2	H_2
Reacting	No	Yes	Yes
$T_0(K)$	700	700	700
$P_0(atm)$	100	100	100
Re_0	2000	850	2500
$M_{c,0}$	0.35	0.35	0.35
Grid points	$3.42 * 10^7$	$3.42 * 10^7$	$1.35 * 10^8$
N_1	384	384	560
N_2	384	384	720
N_3	232	232	336

Table 2.2: Simulation parameters for the supercritical temporally mixing/reacting shear layer database.

Chapter 3

Subgrid analysis

The unclosed terms in Eqs. (1.6) - (1.11) include the filtered heat flux, $\overline{Q_{BK_j}}$, filtered mass flux, $\overline{J_{j,\alpha}}$, and the filtered pressure, $\overline{P(\Psi)}$. The first two terms have recently been disscused by Korucu *et al.* [25] and Foster *et al.* [12]. To study the pressure's effects on the reacting shear layer, the first part of this work is to provide a detailed disscusion of the filtered pressure $\overline{P(\Psi)}$, as it directly influences the flow field and combustion process. More specifically, a detailed comparison of the filtered pressure, $\overline{P(\Psi)}$, and corresponding resolved pressure, $P(\bar{\Psi})$, which is calculated by the filtered primitive variables is conducted. Then this work continues the analyses to the subgrid pressure [$P_{sgs} = \overline{P(\Psi)} - P(\bar{\Psi})$] and to the corresponding gradients of these terms.

However, before beginning the analyses of the filtered pressure, it is first useful to provide a "map" of the flames considered in this study. This is done by plotting pertinent variables as a function of the mixture fraction. These results will further be used to explain consequent results of the filtered pressure analyses. The mixture fraction ϕ is an important parameter in both non-premixed mixing and reacting flows. The mixture fraction is a conserved scalar which singly indicates the relative amount

of mixing present in a flow. Many combustion models are based on the mixture fraction and its relation to product species concentrations and flame temperatures. For present purposes, the mixture fraction is defined as:

$$\phi = \frac{sY^{H_2} - Y^{O_2} + Y_0^{O_2}}{sY_0^{H_2} + Y_0^{O_2}}, \tag{3.1}$$

where $0 \leq \phi \leq 1$, s represents the mass stoichiometry constant and is 0.5 in H_2/O_2 reaction (based on the simplified form $H_2 + 1/2O_2 \rightarrow H_2O$), Y^{H_2} and Y^{O_2} are the local mass fraction values for the fuel (H_2) and oxidizer (O_2), respectively, and $Y_0^{H_2}$ and $Y_0^{O_2}$ are the free stream mass fraction values, respectively. This definition yields the boundary condition for the mixture fraction to be $\phi = 0$ in the pure oxidizer stream, and $\phi = 1$ in the pure fuel stream. Intermediate values correspond to the range of mixed states (see below). The stoichiometric mixture fraction for the H_2/O_2 reaction is ≈ 0.15 (see Fig. 3.1).

Figure 3.1 presents the normalized temperature vs. mixture fraction with a filter width of $\Delta/\delta_{\omega 0} \approx 3$. The maximum flame temperatures occur near the stoichiometric mixture fraction ($0.1 \leq \phi \leq 0.2$), with values near the adiabatic flame temperature. However, in both reacting cases, significant scatter still exists in rich fuel regions ($0.2 \leq \phi \leq 0.5$), indicating that non-equilibrium combustion effects are present in these regions. Figure 3.2 presents the major species mass fraction (Y^{H_2O}, Y^{O_2}, and Y^{H_2}) vs. mixture fraction. The maximum water mass fraction is related to the stoichiometric region, which has little H_2 and O_2. Comparing with the $Re_0 = 850$ reacting case, more significant scatter exists in the $Re_0 = 2500$ reacting case; indicating the enhanced non-equilibrium effects.

The filtered mixture fraction variance, $\widetilde{\phi''^2}$, is one of the more important variables in reacting flow LES modeling. The scatter plots in Fig. 3.3 compare the mixture

fraction variance in the different Reynolds number reacting flows, with a filter size of $\Delta/\delta_{\omega 0} \approx 3.0$. The figure shows that large Reynolds number results in a larger mixture fraction fluctuation. The more developed subgrid scale can be inferred from the larger density of points across the span of the mixture fraction with $Re_0 = 2500$ than $Re_0 = 850$.

The filtered subgrid kinetic energy $\overline{k_{sgs}}$ also gives insight to the extent of development of the subgrid. It is mathematically defined as $\overline{k_{sgs}} = \frac{1}{2}\widetilde{u_i''u_j''}$. Figure 3.4 represents the $\overline{k_{sgs}}$ vs. ϕ, with a filter size of $\Delta/\delta_{\omega 0} \approx 3.0$. The larger magnitude suggests the subgrid turbulence is stronger as the Reynolds number became larger. And the density of data points increases across the span of mixture fraction as the Reynolds number becomes larger; indicating a more "active" subgrid.

Another subgrid variance is the subgrid temperature variance $\widetilde{T''^2}$. As represented in Fig. 3.5, the higher Reynolds number flow has higher subgrid temperature variance. Also, the high temperature variance occurs predominately in the region where $0.1 \leq \phi \leq 0.2$, indicating enhanced subgrid temperature variance along the flame zone.

The filtered subgrid mixture fraction dissipation is also a critical parameter in LES subgrid modeling techniques. It can be mathemetically represented by:

$$\overline{\chi^{\phi}} = \overline{-2J'_{j,\phi}\frac{\partial \phi''}{\partial x_j}}, \tag{3.2}$$

where $J'_{j,\phi}$ is the subgrid mixture fraction diffusion flux vector. Physically, the filtered subgrid mixture fraction dissipation is related to how convoluted the local mixture fraction field is, as well as to the tendency to encounter local extinction and reignition. In LES, the mixutre fraction and its dissipation rate are required to calculate the filtered chemical reaction rate in many models [41, 46, 52, 51, 38]. The scatter plots in

Fig. 3.6 present the filtered subgrid mixture fraction dissipation vs. mixture fraction, with a non-dimensionalized filter width of $\Delta/\delta_{\omega 0} \approx 3.0$. Both the larger maximum value and larger density of points across the span of mixture fraction indicate that stronger turbulence enhances the scalar mixing.

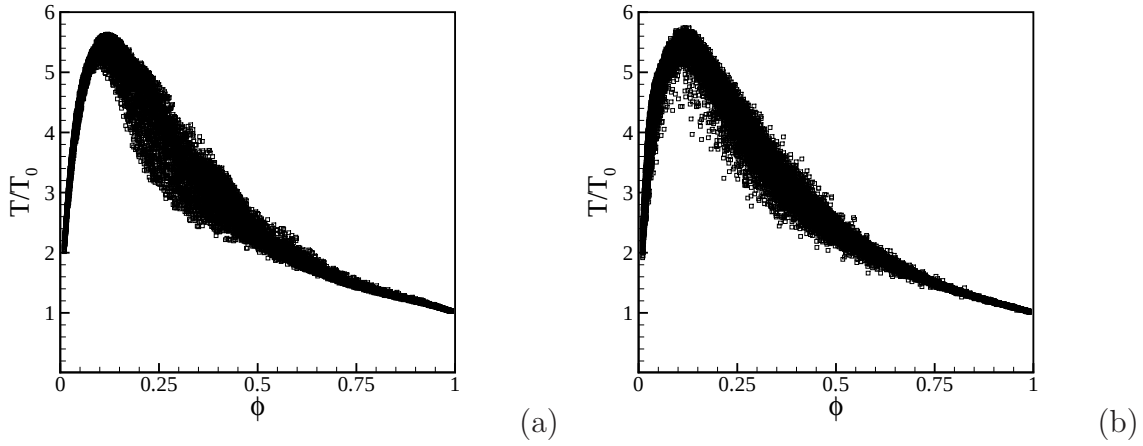

Figure 3.1: Temperature profiles ($T_0 = 700K$) vs. mixture fraction, conditioned on $0.01 \leq \phi \leq 0.99$, $\Delta/\delta_{\omega 0} \approx 3$: (a) $Re_0 = 850$, (b) $Re_0 = 2500$.

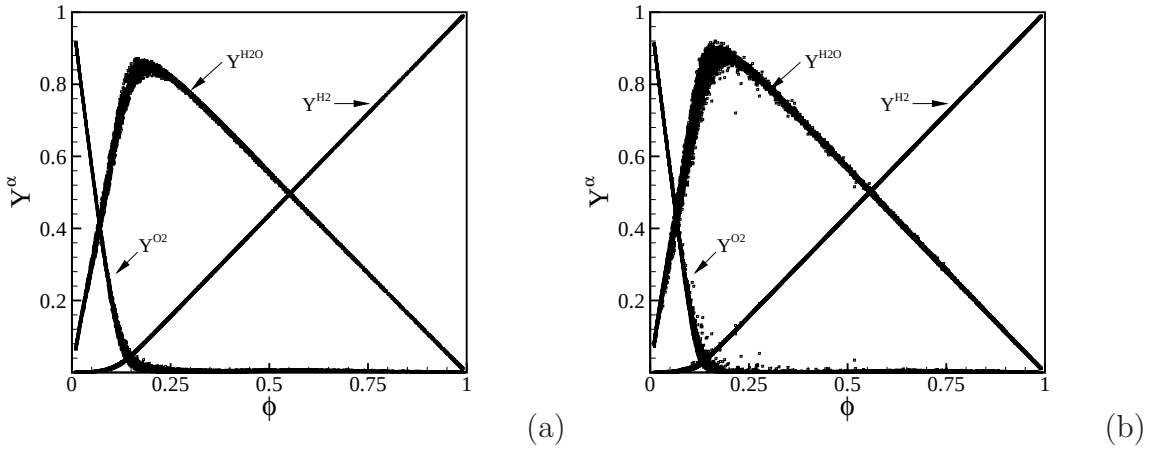

Figure 3.2: Major species mass fractions vs. mixture fraction, conditioned on $0.01 \leq \phi \leq 0.99$, $\Delta/\delta_{\omega 0} \approx 3$: (a) $Re_0 = 850$, (b) $Re_0 = 2500$.

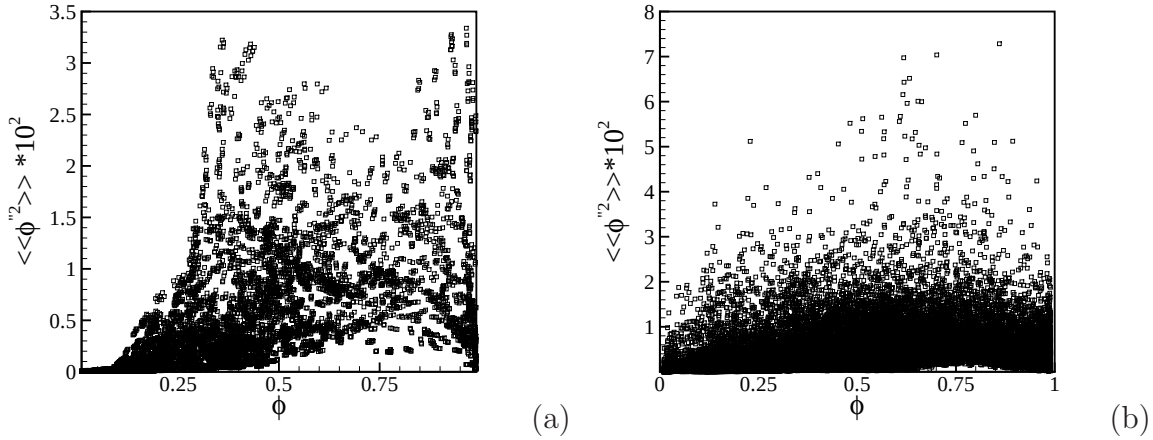

Figure 3.3: Favre filtered mixture fraction variance vs. mixture fraction, conditioned on $0.01 \leq \phi \leq 0.99$, $\Delta/\delta_{\omega 0} \approx 3$: (a) $Re_0 = 850$, (b) $Re_0 = 2500$.

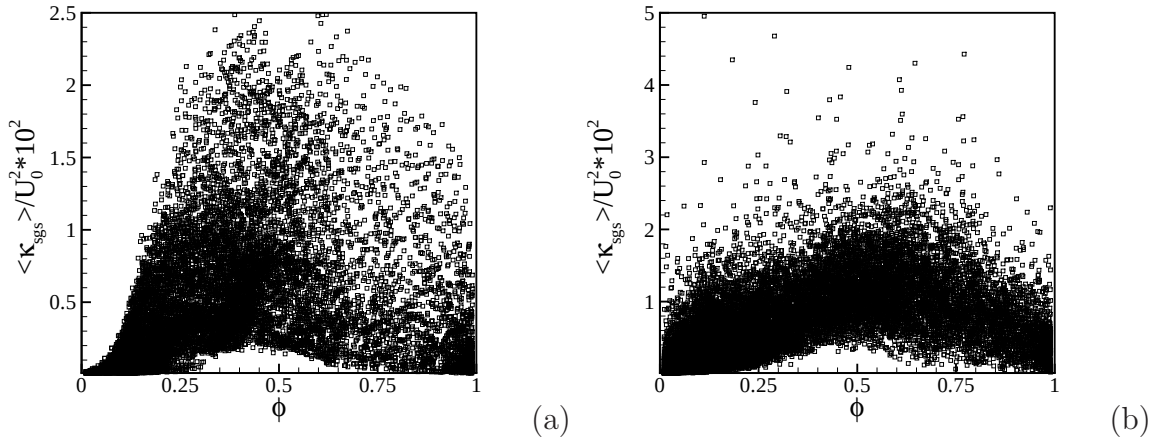

Figure 3.4: Favre filtered kinetic energy vs. mixture fraction, conditioned on $0..01 \leq \phi \leq 0.99$, $\Delta/\delta_{\omega 0} \approx 3$: (a) $Re_0 = 850$, (b) $Re_0 = 2500$.

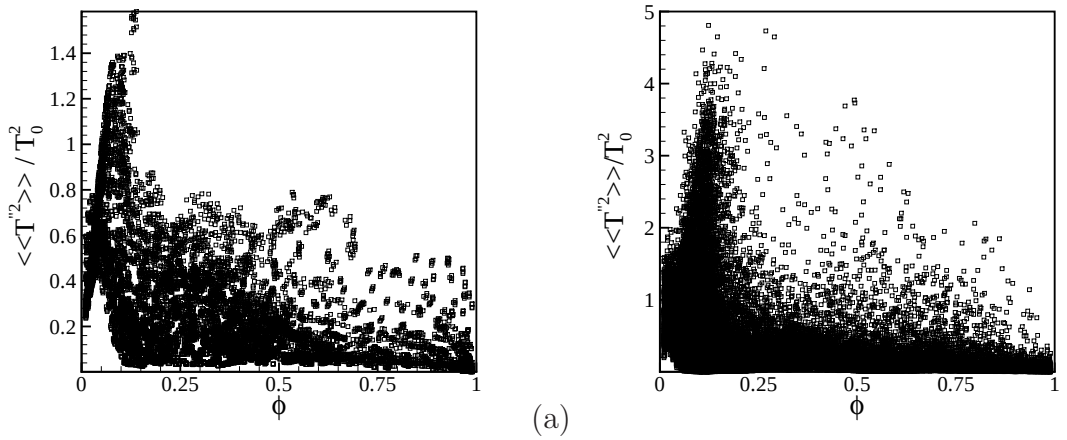

(a) (b)

Figure 3.5: Favre filtered temperature variance vs. mixture fraction, conditioned on $0.01 \leq \phi \leq 0.99$, $\Delta/\delta_{\omega 0} \approx 3$: (a) $Re_0 = 850$, (b) $Re_0 = 2500$.

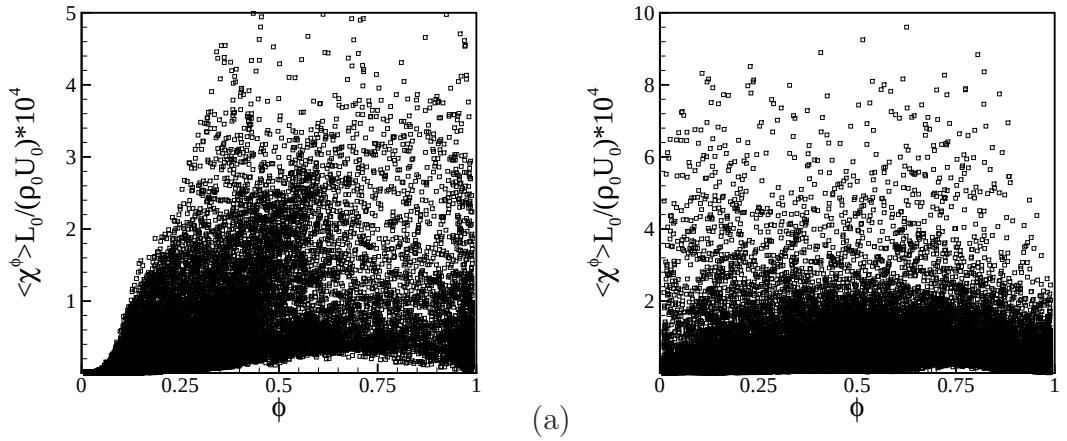

(a) (b)

Figure 3.6: Filtered subgrid mixture fraction dissipation vs. mixture fraction, conditioned on $0.01 \leq \phi \leq 0.99$, $\Delta/\delta_{\omega 0} \approx 3$: (a) $Re_0 = 850$, (b) $Re_0 = 2500$.

3.1 Filtered pressure

There are very few previous studies that address LES modeling analyses for the subgrid pressure in high pressure, turbulent combustion. Most previous studies assumed the filtered pressure, $\overline{P(\Psi)}$, is equal to the resolved pressure, $P(\bar{\Psi})$. However, Selle *et al.* [58] pointed out the potential importance of the difference between these two terms, which is defined as subgrid pressure, in the high pressure binary mixing shear layer. The subgrid analyses for the present work extends Bellan's work into the high pressure reacting shear layer. We begin by a disscusion of the exact filtered pressure, $\overline{P(\Psi)}$, based on the scatter plots of raw data and corresponding correlation coefficients. The filtered pressure is unknown in LES because it requires filtering the pressure calculated by the instanstaneous primitive variable not available from LES, and it may be different from the resolved pressure $P(\bar{\Psi})$.

The following analyses are coducted both "globally" ($0.01 \leq \phi \leq 0.99$, where ϕ is the mixture fraction) and within locally defined regions of the flame. The free stream regions where $\phi \geq 0.99$ and $\phi \leq 0.01$ have much smaller fluctuations than the global region does, therefore they are not considered in this work. The local regions are defined by conditionally filtering on: the stoichiometric conditions ($0.1 \leq \phi \leq 0.2$), elevated temperature regions ($T/T_0 \geq 2$), high OH reaction rate regions $\left(\dot{\omega}^{OH}/E(\dot{\omega}^{OH}) \geq 2\right)$, where $E(\Psi)$ represents the expected value of Ψ within $0.01 \leq \phi \leq 0.99$), regions of high filtered scalar dissipation $\left(\widetilde{\chi^{\phi}}/E(\widetilde{\chi^{\phi}}) \geq 2\right)$, large subgrid kinetic energy $\left(\overline{k_{sgs}}/E(\overline{k_{sgs}}) \geq 2\right)$, large filtered mixture fraction variance $\left(\overline{\phi''^2}/E(\overline{\phi''^2}) \geq 2\right)$, and large temperature variance $\left(\widetilde{T''^2}/E(\widetilde{T''^2}) \geq 2\right)$. The reason chosen for these conditional regions is as follows. As pointed out by Foster *et al.* [10], in combustion the associated scalar gradients can be much larger than in pure mixing, and turbulent flame dynamics are known to be sensitive to local phenomena (temper-

ature variance, mixture fraction variance, dissipartion, etc.), including extinction and reignition. Therefore, a purely global analysis may not be sufficient, and examining those conditional regions mentioned can reveal important information about what is occurring in different regions of the flame.

The raw data of the filtered pressure and resolved pressure are presented in scatter form in Fig. 3.7; conditioned on each specific localized region. The data came from two different flows; one is the mixing flow with $Re = 2000$ shown in the right side figures, the other one is the reacting flow with $Re = 2500$ in the left side figures. The symbol P_f represents the filtered pressure $\overline{P(\Psi)}$ and P_r represents the resovled pressure $P(\bar{\Psi})$. The filter width is $\Delta/\delta_{\omega 0} \approx 3$ in all cases. In the right figures, one can clearly observe that the resolved pressure is nearly identical to the filtered pressure in the mixing flow; the scatters indicates a nearly one to one correspondence between P_r and P_f. However, in the reacting flow, the resolved pressure is significantly different from the filtered pressure. The resolved pressure both overpredicts and underpredicts the filtered pressure; indicating a much more significant subgrid pressure. Figure 3.7(e) indicates that the large filtered temperature variance regions are characterized by large subgrid pressure. Recalling Fig. 3.5, the large Reynolds number results in a larger magnitude and larger zones of subgrid temperature variance. Therefore, in the high Reynolds number reacting flows, the filtered pressure is significantly different from the resolved pressure, which consequently indicates that P_{sgs} may be important for reacting flow LES.

To further study the filtered pressure, this work calculates the corresponding correlation coefficients by the following formula

$$C(P_f, P_r) = \frac{E[(P_{f_i} - E(P_f))\,(P_{r_i} - E(P_r))]}{\sqrt{E[(P_{f_i} - E(P_f))]^2 E[(P_{r_i} - E(P_r))]^2}}, \tag{3.3}$$

where $E(\Psi)$ is the expected value of variable Ψ within the specific conditional regions. Figure 3.8 shows the correlation coefficients of the filtered pressure and resolved pressure calculated for varying filter widths ($\Delta/\delta_{\omega 0} = 0.6, 0.9, 1.4, 3.0$) in both the global and specified local regions. For $\Delta = 0$, the average value of a variable in a zero radial sphere is equal itself (*i.e.* $\bar{\Psi} = \Psi$), therefore the filtered pressure equals the resolved pressure and the correlation coefficients are unity in this limit.

Generally, in most of the conditional regions, as the filter width increases, the correlations decrease; most significantly in the reacting flow with larger Re_0 number. This indicates that as the subgrid becomes more developed, modeling may become required. However, the correlations do not always follow the monotonic trend in some conditional regions in the low Reynolds number reacting flow. For example, Fig. 3.8(a) presents $C(P_f, P_r)$ in the reacting flow with $Re_0 = 850$. In the three conditional regions defined by large filtered subgrid mixture fraction dissipation $\left(\widetilde{\chi^{\phi}}/E(\widetilde{\chi^{\phi}}) \geq 2\right)$, large filtered subgrid kinetic energy $\left(\overline{k_{sgs}}/E(\overline{k_{sgs}}) \geq 2\right)$, and large filtered subgrid mixture fraction variance $\left(\widetilde{\phi''^2}/E(\widetilde{\phi''^2}) \geq 2\right)$, the correlation shows an initial decrease as the filter width increases, followed by a small increase as the filter width increases to approximately larger than $\delta_{\omega 0}$. The reason is explained as follows. According to Figs. 3.3, 3.4, and 3.6, the regions of large filtered subgrid mixture fraction variance, subgrid kinetic energy, and subgrid mixture fraction dissipation are predominatly within the rich side of the stoichiometric condition ($\phi \geq 0.25$). As the filter width increases to relatively large values, the filtering operation includes a larger portion of free stream points where the primitive variable variances are small, which consequently increases the correlations. However, we cannot see this "jump" in large Re_0 number case. Because with the larger Re_0 number, the turbulence is more developed across the flame region, as a result, there are less "smooth" flow regions which would increase the coefficients. However one can still observe that the correlations decrease

much more slowly in the three conditional regions mentioned above.

On the other hand, the decreasing levels of the coefficients vary accroding to the different conditional flame regions. The strongest dependence of correlation coefficients on filter width is found in the region corresponding to high OH reaction rate. The lowest correlations (≈ 0.55 for $Re_0 = 850$, and ≈ 0.3 for $Re_0 = 2500$) are found when the largest filter width is applied in the high OH reaction rate region, suggesting that subgrid contributions are most important along the flame front. Also, the second strongest relation between correlation coefficient and filter width is found in the region with large filtered subgrid temperature variance. This is not surpringsing because the temperature directly and implicitly appears in both the two terms in the right hand side of the Peng-Robison state equation.

3.2 Subgrid pressure

As disscused in the last chapter, the filtered pressure does not necessarily equal the resolved pressure for reacting flows. Therefore, an analysis of the difference between $\overline{P(\Psi)}$ and $P(\bar{\Psi})$, which is defined as the subgrid pressure P_{sgs}, is needed both in the global region and conditional regions. To quantify the subgrid pressure, Fig. 3.9 presents the probability density functions (PDFs) of the ratios of the absolute value of the subgird pressure, P_{sgs}, to the filtered pressure, $\overline{P(\Psi)}$, with a filter width of $\Delta/\Delta_1 = 25$, in each conditional region for the three different flows. All the plots display wider curves in the reacting cases than in the mixing cases, indicating the subgrid pressure is more significant because of the chemical reaction. In addition, the PDFs are similar in the two different reacting Reynolds numbers, indicating the subgrid pressure may be relatively insensitive to the Reynolds number.

The PDF curves of Fig. 3.9 are not delta functions at $P_{sgs}/P_f = 0$; indicating

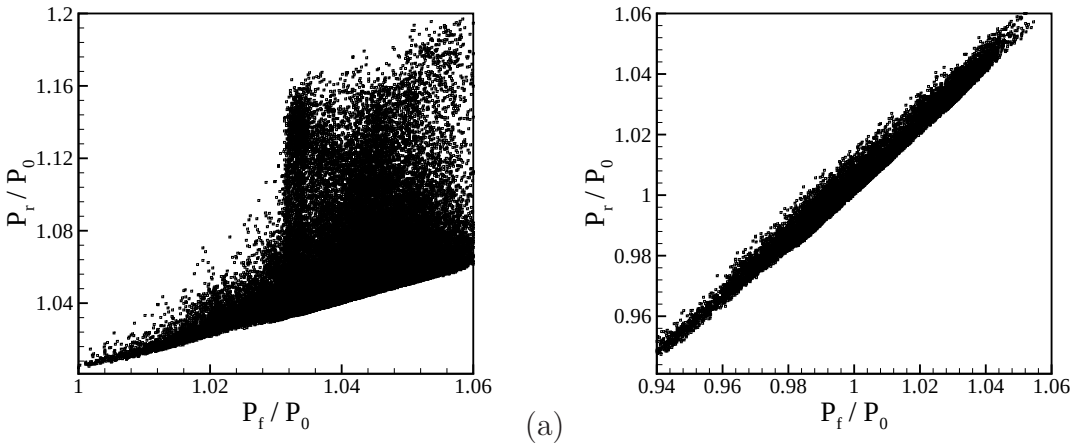
1.2
1.16
1.12
1.08
1.04
P_r / P_0
1
1.02
1.04
1.06
P_f / P_0
1.06
1.04
1.02
1
0.98
0.96
P_r / P_0
0.94
0.96
0.98
1
1.02
1.04
1.06
P_f / P_0

(a)

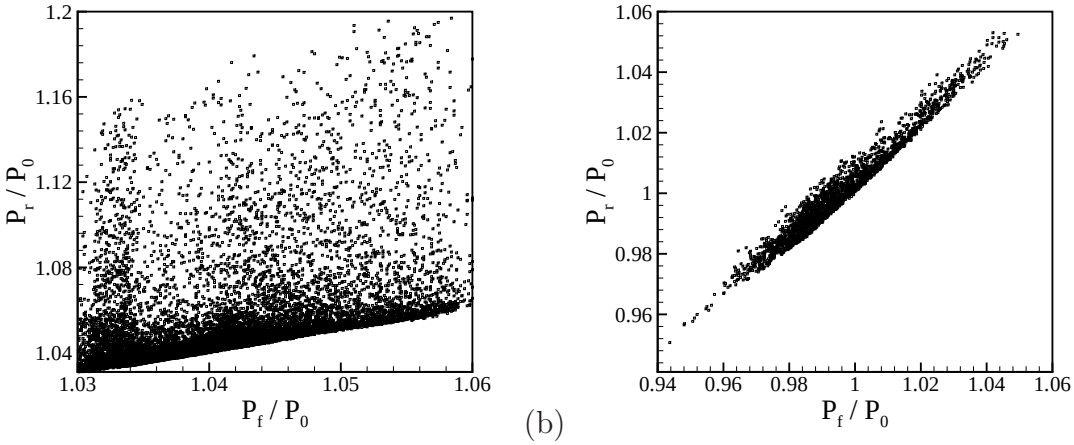
1.2
1.16
1.12
1.08
1.04
P_r / P_0
1.03
1.04
1.05
1.06
P_f / P_0
1.06
1.04
1.02
1
0.98
0.96
P_r / P_0
0.94
0.96
0.98
1
1.02
1.04
1.06
P_f / P_0

(b)

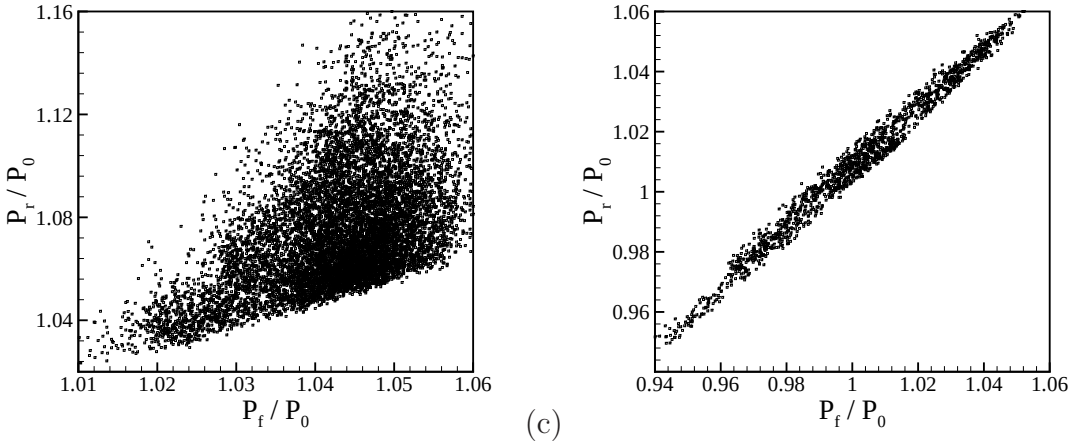
1.16
1.12
1.08
1.04
P_r / P_0
1.01
1.02
1.03
1.04
1.05
1.06
P_f / P_0
1.06
1.04
1.02
1
0.98
0.96
P_r / P_0
0.94
0.96
0.98
1
1.02
1.04
1.06
P_f / P_0

(c)

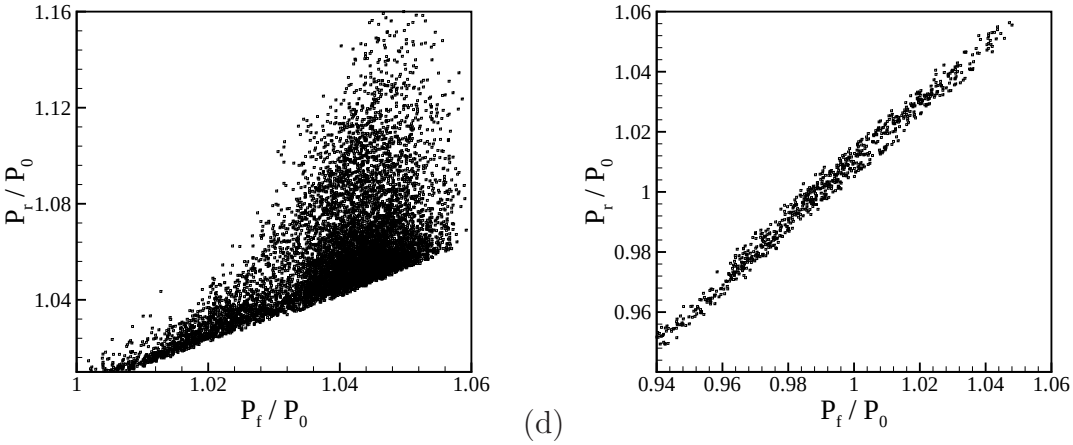
1.16
1.12
1.08
1.04
P_r / P_0
1
1.02
1.04
1.06
P_f / P_0
1.06
1.04
1.02
1
0.98
0.96
P_r / P_0
0.94
0.96
0.98
1
1.02
1.04
1.06
P_f / P_0

(d)

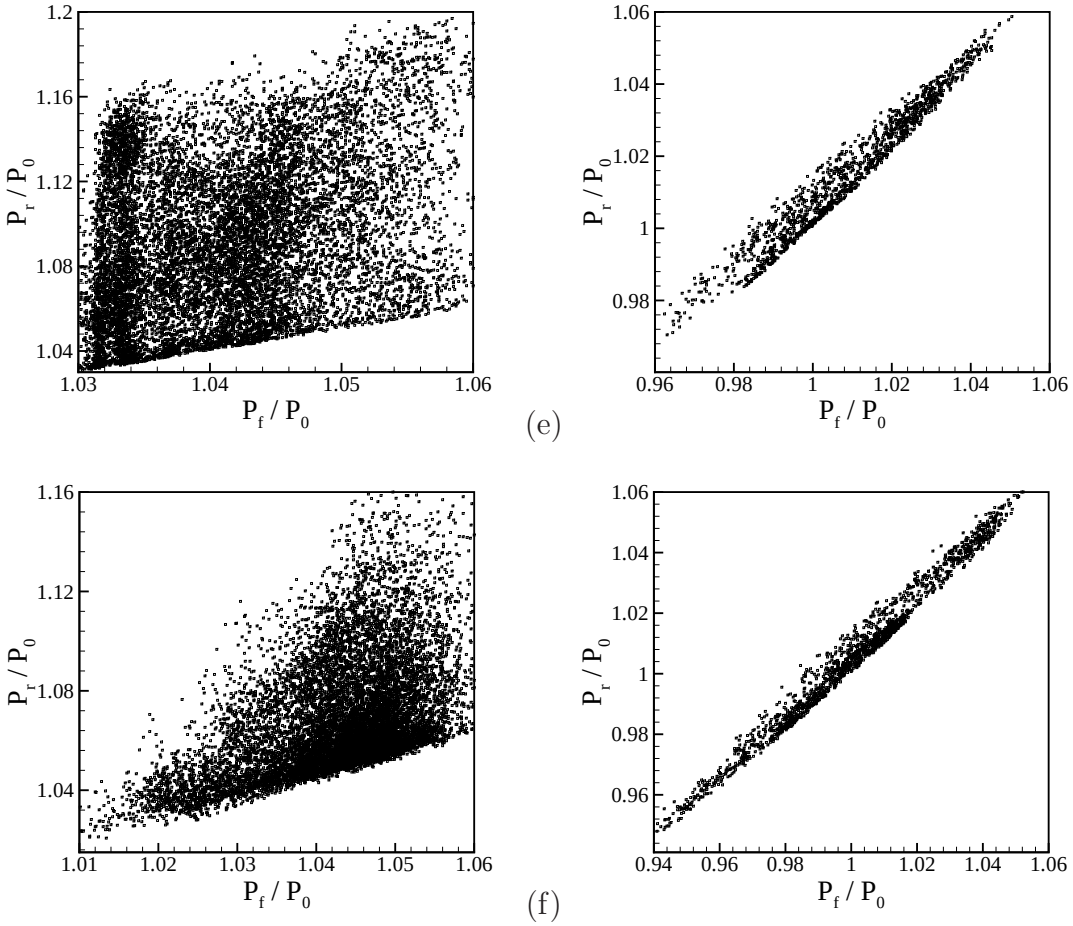

Figure 3.7: Scatter plots of P_f vs. P_r. The left side figures are reacting cases with $Re_0 = 2500$, while the right side figures are for the mixing case with $Re_0 = 2000$, $\Delta/\delta_{\omega 0} \approx 3$, conditioned on: (a) $0.01 \leq \phi \leq 0.99$, (b) $0.1 \leq \phi \leq 0.2$, (c) $\widetilde{\chi^{\phi}}/E(\widetilde{\chi^{\phi}}) \geq 2$, (d) $\overline{k_{sgs}}/E(\overline{k_{sgs}}) \geq 2$, (e) $\widetilde{T''^2}/E(\widetilde{T''^2}) \geq 2$, (f) $\widetilde{\phi''^2}/E(\widetilde{\phi''^2}) \geq 2$.

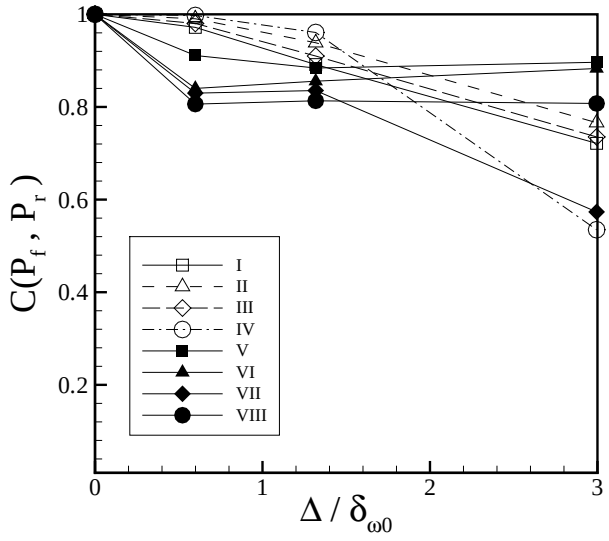

(a)

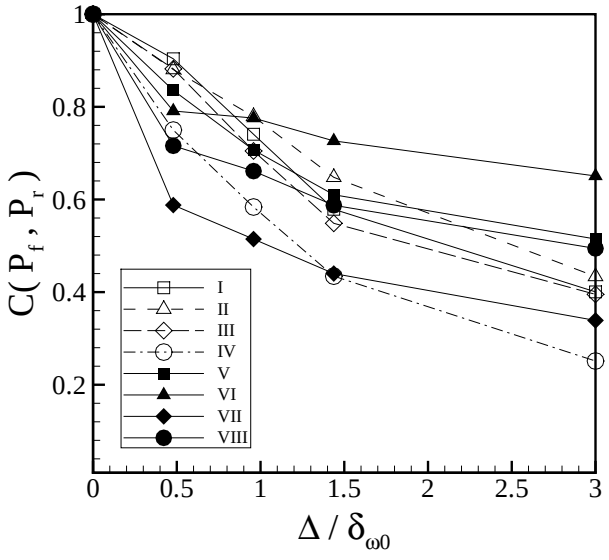

(b)

Figure 3.8: Correlation coefficients C(P_f, P_r) as a function of filter width, for reacting cases, with (a) $Re_0 = 850$ and (b) $Re_0 = 2500$, conditioned on: (I) $0.01 \leq \phi \leq 0.99$, (II) $0.1 \leq \phi \leq 0.2$, (III) $T/T_0 \geq 2$, (IV) $\dot{\omega}^{OH}/E(\dot{\omega}^{OH}) \geq 2$, (V) $\widetilde{\chi^{\phi}}/E(\widetilde{\chi^{\phi}}) \geq 2$, (VI) $\overline{k_{sgs}}/E(\overline{k_{sgs}}) \geq 2$, (VII) $\widetilde{T''^2}/E(\widetilde{T''^2}) \geq 2$, and (VIII) $\widetilde{\phi''^2}/E(\widetilde{\phi''^2}) \geq 2$.

non-zero subgrid pressure values exist. However, in all cases the PDFs, are limited to values only of order a few percent. Nevertheless, trends are apparent when examining the locally conditioned regions. Near the stoichiometric region [Fig. 3.9(b)], large filtered kinetic energy region [Fig. 3.9(d)], and large filtered temperature variance region [Fig. 3.9(e)], the PDFs are similar in shape, with the peaks near zero and relatively narrow widths. For the regions of large filtered subgrid mixture fraction dissipation [Fig. 3.9(c)] and large filtered mixture fraction variance [Fig. 3.9(f)], the reacting cases have asymmetric PDFs curves towards larger ratios of $|P_{sgs}|/\overline{P(\Psi)}$. The span of the ratios of $|P_{sgs}|$ and $\overline{P(\Psi)}$ is wider; indicating the magnitude of subgrid pressure is significantly related to the mixture fraction variance and the subgrid mixture fraction dissipation. However, the difference between the filtered pressure and the resolved pressure is not very significant in this perspective, because the majority of ratios of $|P_{sgs}|$ and $\overline{P(\Psi)}$ fall in the range of $\sim 1\%$ in the mixing case and $\sim 1-13\%$ in the reacting cases.

Although the subgrid pressure is relatively small compared with the resolved pressure, we still cannot simply neglect it, because the subgrid pressure influences the flow field by its gradient $[\frac{\partial P_{sgs}}{\partial x_i} = \frac{\partial \overline{P(\Psi)} - P(\bar{\Psi})}{\partial x_i}]$. In particular, even if the subgrid pressure, $P_{sgs} = \overline{P(\Psi)} - P(\bar{\Psi})$, can be neglected, the subgrid pressure gradient, $\partial P_{sgs}/\partial x_i$, may be much more significant as differentiation enhances small scale features. Selle *et al.* [58] have suggested that the subgrid pressure gradient could contain 50% of the resolved pressure gradient in a binary mixing shear layer. This work furthers the analysis to reacting shear layers.

Figure 3.10 presents the PDFs of the ratios of the magnitude of the subgrid pressure gradient to the magnitude of the resolved pressure gradient in each of the conditional regions, with a filter width of $\Delta/\delta_{\omega 0} \approx 3$. Ideally, from a modeling perspective, the subgrid pressure would be small enough to be neglected, [*i.e.*

$|\frac{\partial P_{sgs}}{\partial x_i}|/|\frac{\partial P(\bar{\Psi})}{\partial x_i}| = 0]$. However, all plots display a wide distribution across the ratios of $|\frac{\partial P_{sgs}}{\partial x_i}|/|\frac{\partial P(\bar{\Psi})}{\partial x_i}|$. The peaks are located at ≈ 0.25 in the mixing flow and ≈ 1.0 in the reacting flows, suggesting a similar magnitude between the subgrid pressure gradient and the resolved pressure gradient. These PDF curves indicate that the subgrid pressure gradient is significant and can be $\approx 40\%$ of the resolved pressure gradient in the mixing case (similar to the results obtained in [58]). It is even larger in the two reacting cases, because the chemical reaction generates larger scalar gradients than in the purely mixing case. On the other hand, the PDFs are similar in different Reynolds number reacting flows. It is not surprising, because as presented in Fig. 3.9, for different Reynolds number reacting flows, the PDFs of the ratios of P_{sgs}/P_r are similar. Hence, the Reynolds number does not influence the subgrid pressure gradient significantly.

For the regions related to the stoichiometric mixture fraction ($0.1 \leq \phi \leq 0.2$), large filtered subgrid mixture fraction dissipation ($\overline{\chi^\alpha}/E(\overline{\chi^\alpha}) \geq 2$), large kinetic energy $\left(\overline{k_{sgs}}/E(\overline{k_{sgs}}) \geq 2\right)$, and large filtered mixture fraction variance $\left(\widetilde{\phi''^2}/E(\widetilde{\phi''^2}) \geq 2\right)$ [Fig. 3.10(b), (c), (d), and (f)], the PDFs display similar shapes. There are only small differences in width and magnitude; indicating the subgrid pressure distributions are similar in these conditional regions. However, in contrast, the region corresponding to the large filtered subgrid temperature variance $\left(\widetilde{T''^2}/E(\widetilde{T''^2}) \geq 2\right)$ [Fig. 3.10(e)] displays much narrower PDFs with higher peaks again; implying the subgrid temperature variance has an important contribution to the subgrid pressure gradient.

To further study the subgrid pressure gradient in each flow direction, Fig. 3.11 presents the PDF of the ratios of the subgrid pressure gradient component to the resolved pressure gradient component, in the reacting flow ($Re_0 = 2500$), with a filter width $\Delta/\Delta_1 = 25$ ($\Delta/\delta_{\omega 0} \approx 3$). Similiar to the trend in Fig. 3.10, the subgrid pressure gradient is of the same order or larger than the resolve pressure gradient in all flow

directions. One new observation is that the majority of the flow is dominated by components of the subgrid pressure gradient in the opposite direction to those of the resolved pressure gradient. This may be due to the fact that, in most flame regions, the resolved pressure overpredicts the filtered pressure (Fig. 3.7), therefore the resolved pressure gradient is larger than the filtered pressure gradient and $\frac{\partial P_f}{\partial x_i} - \frac{\partial P_r}{\partial x_i} = \frac{\partial P_{sgs}}{\partial x_i} \leq 0$. However, this remainsspeculative, and this issue is worthy of further investigation.

The subgrid pressure gradient is perhaps more importantly compared with the subgrid turbulent stress divergence from a modeling perspective. Figure 3.12 presents the PDFs of the ratio of the magnitude of the subgrid pressure gradient, $|\frac{\partial P_{sgs}}{\partial x_i}|$, to the magnitude of the subgrid turbulent stress divergence, $|\frac{\partial \Pi_{ij}}{\partial x_j}|$, with a filter width of $\Delta/\Delta_1 = 25$. The global view of the mixing layer, $0.01 \leq \phi \leq 0.99$ [Fig. 3.12(a)], shows that the subgrid pressure gradient is larger than the subgrid turbulent stress divergence in all three different flows. The peaks are located at ≈ 0.5 in the mixing case and ≈ 2 in the reacting cases. The PDF curves have asymmetric distributions skewed towards large ratio of $|\frac{\partial P_{sgs}}{\partial x_i}|/|\frac{\partial \Pi_{ij}}{\partial x_j}|$; further suggesting the importance of the subgrid pressure. However, there is not a monotonic relation between the ratio of $|\frac{\partial P_{sgs}}{\partial x_i}|/|\frac{\partial \Pi_{ij}}{\partial x_j}|$ and the Reynolds number. For larger Reynolds number, the subgrid pressure gradient becomes relatively larger in the stoichiometric regions [$0.1 \leq \phi \leq 0.2$, Fig. 3.12(b)], but smaller in the regions related to the large filtered subgrid mixture fraction dissipation [$\overline{\chi^\phi}/E(\overline{\chi^\phi}) \geq 2$, Fig. 3.12(c)] and large filtered subgrid temperature variance [$\widetilde{T''^2}/E(\widetilde{T''^2}) \geq 2$, Fig. 3.12(e)], and barely changing in the other two regions [Fig. 3.12(d) and (f)]. This may be due to the fact that although the subgrid scales are more developed for larger Reynolds numbers, the subgrid pressure gradient may not increase as much as the subgrid turbulent stress divergence in all regions.

Tables 3.1, 3.2 and 3.3 continue the comparison of the subgrid pressure gradient

components relative to other terms in the LES momentum equations. The magnitude of each term in the momentum equation is calculated based on the L2 norm ($||x|| = \sqrt{\Sigma x_k^2/n}$), as used in previous research [58, 63]. This analysis is conducted in the global region, where $0.01 \leq \phi \leq 0.99$, with two filter widths: $\Delta/\delta_{\omega 0} \approx 0.6$ and $\Delta/\delta_{\omega 0} \approx 3$. The results show that, in the mixing case, the subgrid pressure gradient is at least of the same order as other terms [*ie.* as presented in Table. 3.3, it is $\approx 60\%$ of $\frac{\partial \Pi_{3j}}{\partial x_j}$, and $\approx 12\%$ of $\frac{\partial \bar{\rho}\widetilde{u_1}\widetilde{u_j}}{\partial x_j}$, with $\Delta/\delta_{\omega 0} \approx 0.6$,]. When the chemical reaction is involved, the subgrid pressure gradient becomes even larger, (*ie.* as presented in Table. 3.3, for the $Re_0 = 2500$ reacting case, the subgrid pressure gradient significantly increases to almost twice the inertial term). This suggests that the subgrid pressure gradient is significant and may need to be modeled in an actual LES. In addition, the results show that the subgrid pressure gradient is significantly dependent on the filter size. For example, in Table. 3.1, for the reacting case with $Re_0 = 2500$, as the filter width increases, the subgrid pressure gradient $\frac{\partial P_{sgs}}{\partial x_i}$ increases from $\approx 80\%$ to $\approx 95\%$ of $\frac{\partial P(\bar{\Psi})}{\partial x_i}$ and from $\approx 20\%$ to $\approx 45\%$ of the leading term, $\frac{\partial \bar{\rho}\widetilde{u_1}\widetilde{u_j}}{\partial x_j}$.

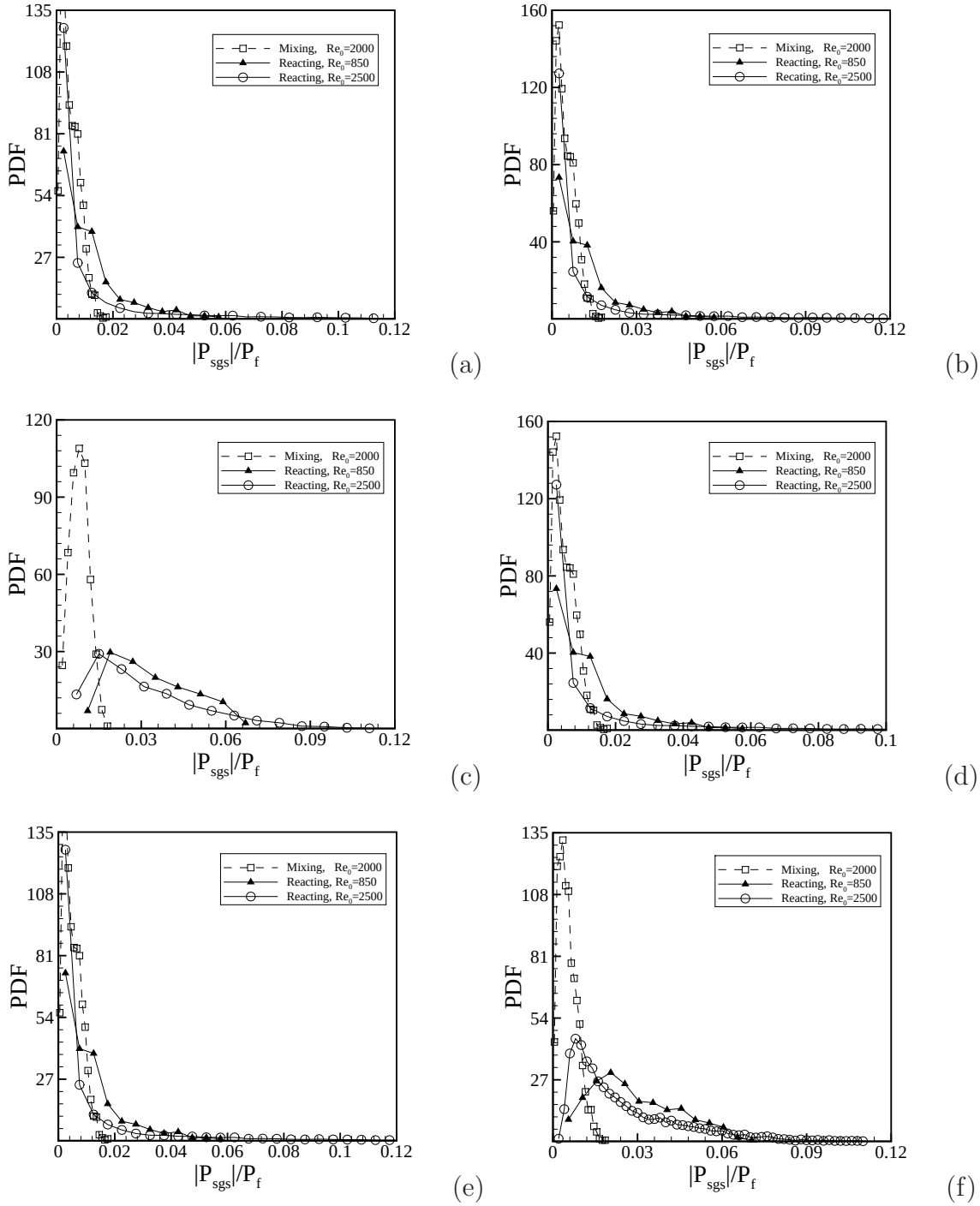

Figure 3.9: PDFs of the ratios of $|P_{sgs}|/\overline{P(\Psi)}$, $\Delta/\delta_{\omega 0} \approx 3$, conditioned on: (a) $0.01 \leq \phi \leq 0.99$, (b) $0.1 \leq \phi \leq 0.2$, (c) $\overline{\chi^{\phi}}/E(\overline{\chi^{\phi}}) \geq 2$, (d) $\overline{k_{sgs}}/E(\overline{k_{sgs}}) \geq 2$, (e) $\widetilde{T''^2}/E(\widetilde{T''^2}) \geq 2$, (f) $\widetilde{\phi''^2}/E(\widetilde{\phi''^2}) \geq 2$.

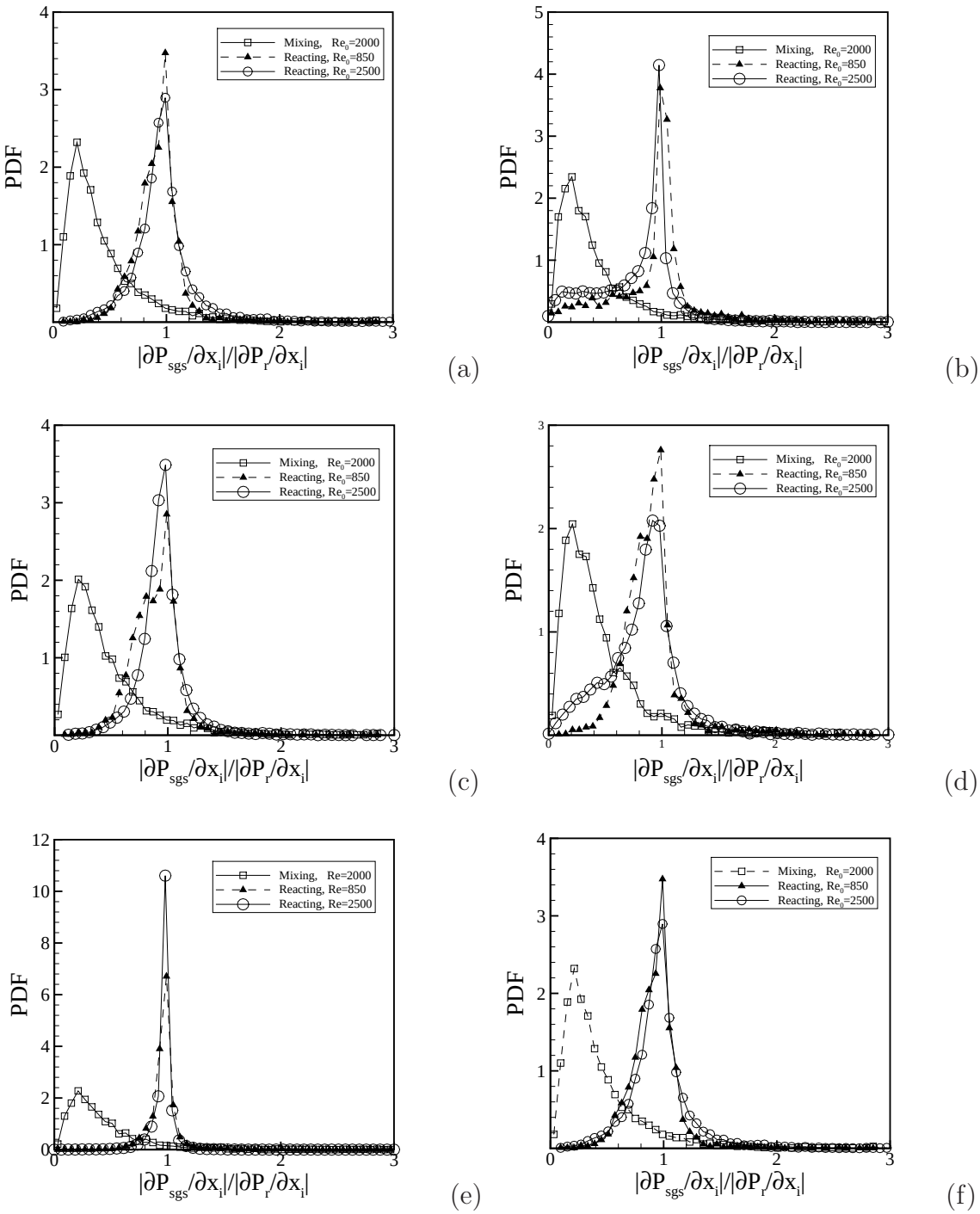

Figure 3.10: PDFs of the ratios of $|\frac{\partial P_{sgs}}{\partial x_i}|/|\frac{\partial P(\bar{\Psi})}{\partial x_i}|$, $\Delta/\delta_{\omega 0} \approx 3$, conditioned on: (a) $0.01 \leq \phi \leq 0.99$, (b) $0.1 \leq \phi \leq 0.2$, (c) $\overline{\chi^{\phi}}/E(\overline{\chi^{\phi}}) \geq 2$, (d) $\overline{k_{sgs}}/E(\overline{k_{sgs}}) \geq 2$, (e) $\widetilde{T''^2}/E(\widetilde{T''^2}) \geq 2$, (f) $\widetilde{\phi''^2}/E(\widetilde{\phi''^2}) \geq 2$.

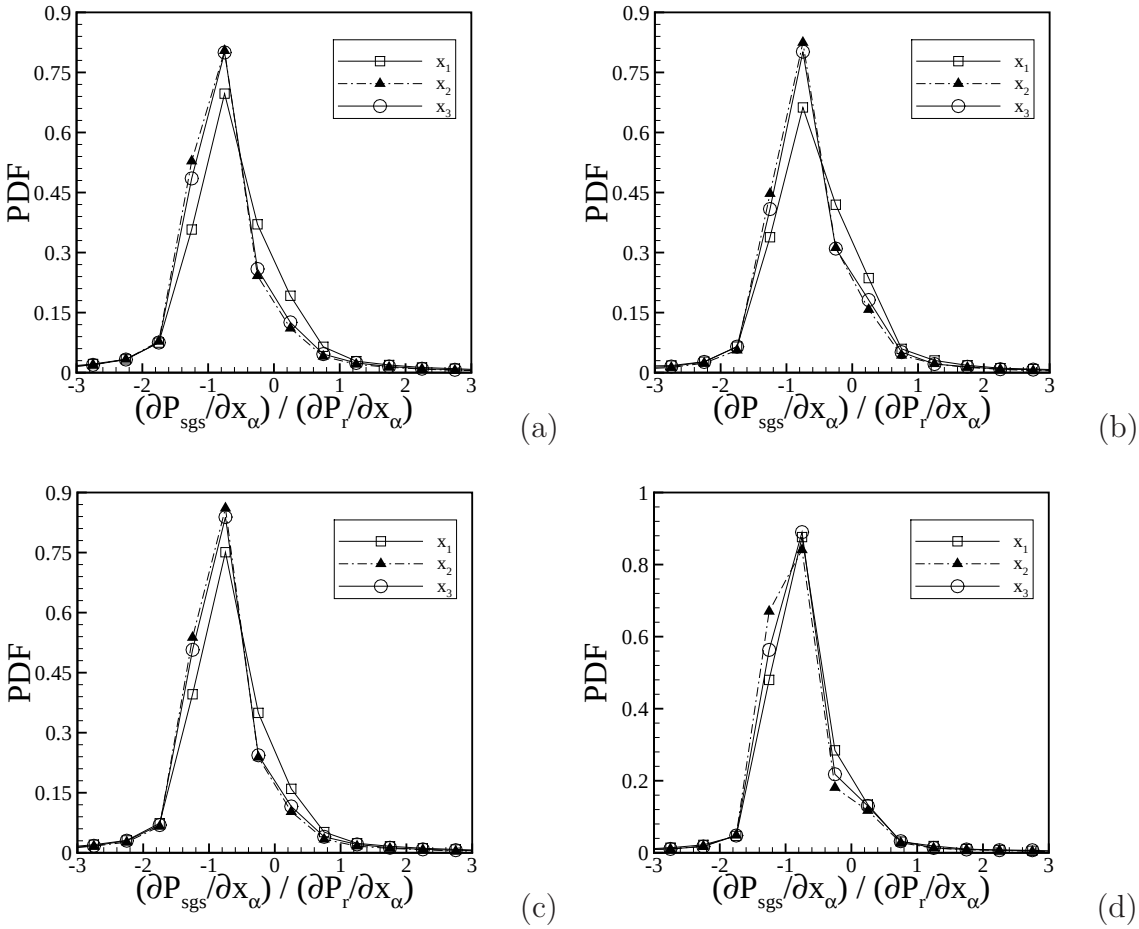
PDF
$(\partial P_{sgs}/\partial x_\alpha) / (\partial P_r/\partial x_\alpha)$
x_1
x_2
x_3
(a)
(b)
(c)
(d)

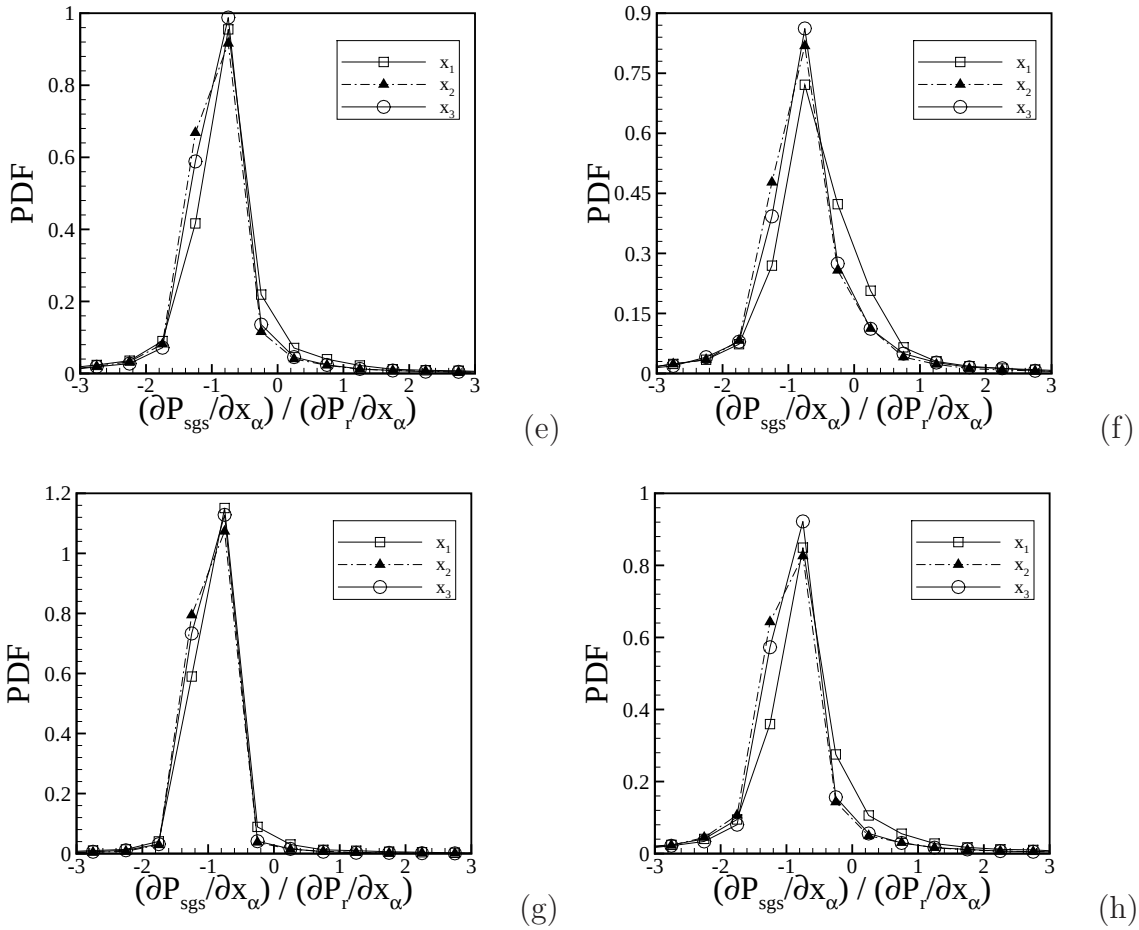

Figure 3.11: PDFs of the ratios of $\frac{\partial P_{sgs}}{\partial x_\alpha} / \frac{\partial P(\bar{\Psi})}{\partial x_\alpha}$ for the reacting case with $Re_0 = 2500$, $\Delta/\delta_{\omega 0} \approx 3$, conditioned on: (a) $0.01 \leq \phi \leq 0.99$, (b) $0.1 \leq \phi \leq 0.2$, (c) $T/T_0 \geq 2$, (d) $\dot{\omega}^{OH}/E(\dot{\omega}^{OH}) \geq 2$, (e) $\overline{\chi^\phi}/E(\overline{\chi^\phi}) \geq 2$, (f) $\overline{k_{sgs}}/E(\overline{k_{sgs}}) \geq 2$, (g) $\widetilde{T''^2}/E(\widetilde{T''^2}) \geq 2$, (h) $\widetilde{\phi''^2}/E(\widetilde{\phi''^2}) \geq 2$.

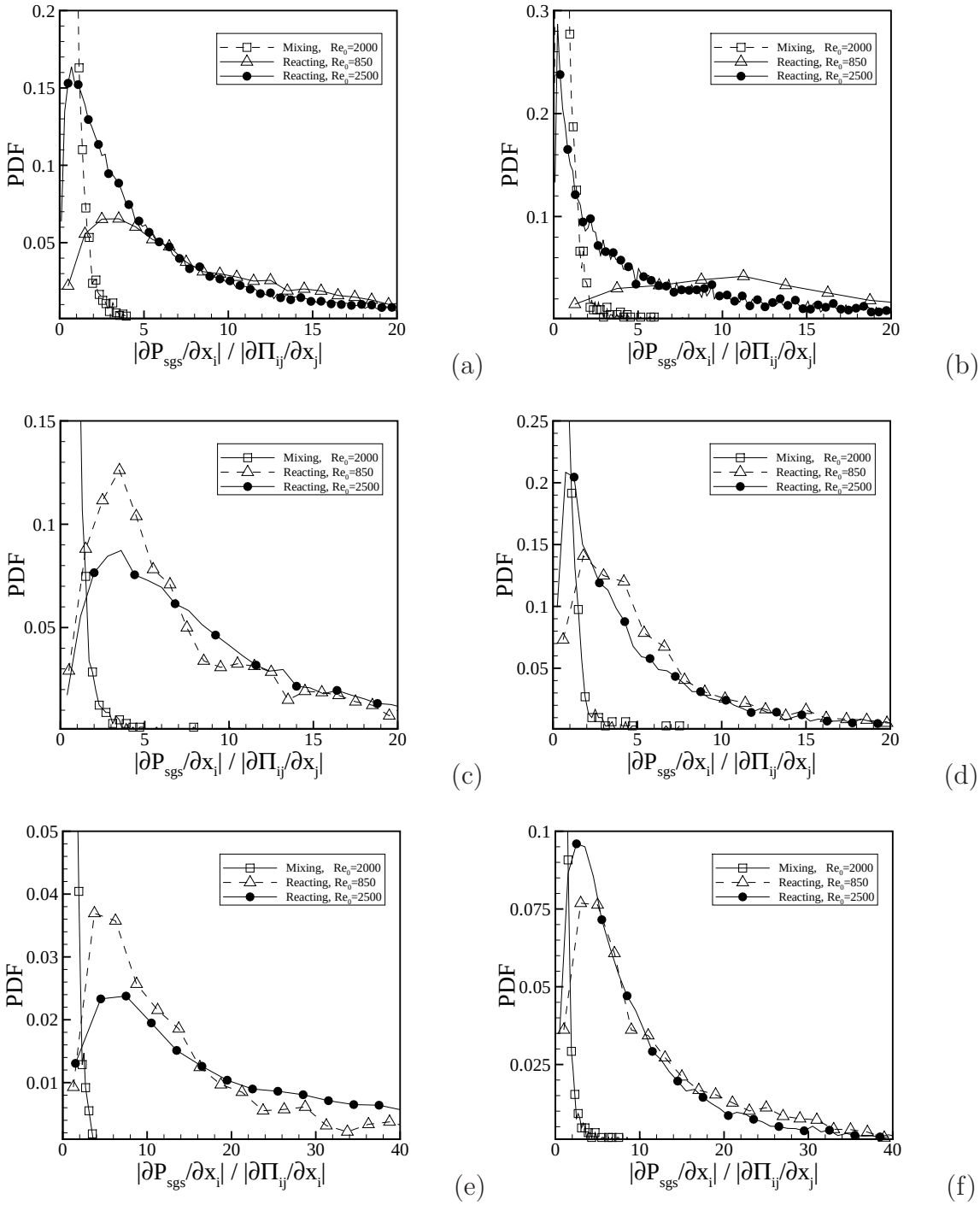

Figure 3.12: PDFs of the ratios of $|\frac{\partial P_{sgs}}{\partial x_i}|/|\frac{\partial \Pi_{ij}}{\partial x_j}|$, $\Delta/\delta_{\omega 0} \approx 3$, conditioned on: (a) $0.01 \leq \phi \leq 0.99$, (b) $0.1 \leq \phi \leq 0.2$, (c) $\overline{\chi^{\phi}}/E(\overline{\chi^{\phi}}) \geq 2$, (d) $\overline{k_{sgs}}/E(\overline{k_{sgs}}) \geq 2$, (e) $\widetilde{T''^2}/E(\widetilde{T''^2}) \geq 2$, (f) $\widetilde{\phi''^2}/E(\widetilde{\phi''^2}) \geq 2$.

	$\Delta/\delta_{\omega 0} \approx 0.6$			$\Delta/\delta_{\omega 0} \approx 3.0$		
x_1 ***momentum***	***MIX***1	***REACT***1	***REACT***2	***MIX***1	***REACT***1	***REACT***2
$\frac{\partial \bar{\rho}\tilde{u}_1\tilde{u}_j}{\partial x_j}$	63.66	8.68	36.32	13.47	5.58	19.51
$\frac{\partial P_r\delta_{1j}}{\partial x_j}$	19.72	4.73	8.23	6.31	7.08	9.93
$\frac{\partial \tilde{\tau}_{1j}}{\partial x_j}$	1.89	4.69	1.21	0.41	2.11	0.45
$\frac{\partial \Pi_{1j}}{\partial x_j}$	8.19	2.22	1.61	4.16	1.57	1.27
$\frac{\partial P_{sgs}\delta_{1j}}{\partial x_j}$	2.13	2.21	6.82	1.03	5.61	9.48

Table 3.1: L2 norm of components of the LES momentum equations. All values are non-dimensionalized by $P_0/\delta_{\omega 0} * 10^{-3}$.

	$\Delta/\delta_{\omega 0} \approx 0.6$			$\Delta/\delta_{\omega 0} \approx 3.0$		
x_2 ***momentum***	***MIX***1	***REACT***1	***REACT***2	***MIX***1	***REACT***1	***REACT***2
$\frac{\partial \bar{\rho}\tilde{u}_2\tilde{u}_j}{\partial x_j}$	41.55	5.11	13.13	7.89	2.29	4.18
$\frac{\partial P_r\delta_{2j}}{\partial x_j}$	18.40	7.30	12.09	4.81	16.51	17.86
$\frac{\partial \tilde{\tau}_{2j}}{\partial x_j}$	1.76	3.20	0.98	0.31	1.35	0.29
$\frac{\partial \Pi_{2j}}{\partial x_j}$	6.76	1.56	1.36	3.83	1.74	1.02
$\frac{\partial P_{sgs}\delta_{2j}}{\partial x_j}$	2.61	4.52	10.80	1.79	15.73	17.68

Table 3.2: L2 norm of components of the LES momentum equations. All values are non-dimensionalized by $P_0/\delta_{\omega 0} * 10^{-3}$.

	$\Delta/\delta_{\omega 0} \approx 0.6$			$\Delta/\delta_{\omega 0} \approx 3.0$		
x_3 ***momentum***	***MIX***1	***REACT***1	***REACT***2	***MIX***1	***REACT***1	***REACT***2
$\frac{\partial \bar{\rho}\tilde{u}_3\tilde{u}_j}{\partial x_j}$	40.32	3.283	13.18	4.23	1.02	3.05
$\frac{\partial P_r\delta_{3j}}{\partial x_j}$	19.42	25.03	25.62	3.64	13.35	16.18
$\frac{\partial \tilde{\tau}_{3j}}{\partial x_j}$	1.77	3.28	1.11	0.22	1.03	0.26
$\frac{\partial \Pi_{3j}}{\partial x_j}$	8.98	1.62	1.84	3.50	1.18	1.24
$\frac{\partial P_{sgs}\delta_{3j}}{\partial x_j}$	5.30	25.97	25.03	2.02	13.30	15.96

Table 3.3: L2 norm of components of the LES momentum equations. All values are non-dimensionalized by $P_0/\delta_{\omega 0} * 10^{-3}$.

Chapter 4

Subgrid Model

4.1 Motivation

The subgrid pressure, P_{sgs}, which is the difference between the filtered pressure and the resolved pressure [$P_{sgs} = \overline{P(\Psi)} - P(\bar{\Psi})$], is an unknown term in the LES momentum equation, Eq. (1.7). As concluded in the last chapter, it is significant in reacting flows and may need to be modeled in LES.

One of the most frequently used modeling technique in LES is the eddy-viscosity method. The simplest linear eddy-viscosity model is the Smagorinsky model (1963), which was originally used to model the subgrid turbulent stress τ_{ij}:

$$\Pi_{ij} = -2\nu_r \bar{S}_{ij}, \tag{4.1}$$

$$\nu_r = C_s(\Delta)^2 |\bar{S}|, \tag{4.2}$$

$$\bar{S}_{ij} = \frac{1}{2}\left(\frac{\partial \bar{u}_i}{\partial x_j} + \frac{\partial \bar{u}_j}{\partial x_i}\right), \qquad |\bar{S}| = 2(\bar{S}_{ij}\bar{S}_{ij})^{\frac{1}{2}} \tag{4.3}$$

where $\bar{S}_{ij}$ is the filtered strain rate, ν_r the eddy viscosity of the resolved flow field, and

the Smagorinsky coefficient is C_s. This model is analogous to the gradient diffusion hypothesis widely used in RANS as a model for the Reynolds stress tensor. In the original "Smagorinsky model", C_s was taken to be a constant ~ 0.1. The main drawback of the Smagorinsky model is that the ν calculated by the Eq. 4.2 is always positive, and therefore, it cannot account for the local backscatter. The eddy viscosity model is also very poorly correlated with the actual subgrid stresses.

Therefore, a "scale-similarity" model has been proposed. The scale-similarity model is based on the assumption that the most active subgrid scales are those closest to the cutoff wavenumber, and that the scales with which they interact are those immediately above the cutoff wave number (Bardina *et al.*, 1980 [1]). Bardina *et al.* [1] suggest calculating the subgrid stresses as:

$$\Pi_{ij} = C_L(\widetilde{\bar{u}_i\bar{u}_j} - \tilde{\bar{u}}_i\tilde{\bar{u}}_j) \tag{4.4}$$

where $\tilde{\bar{\Delta}}$ represents a larger filter width (*eg.* $\tilde{\bar{\Delta}} = \sqrt{2}\bar{\Delta}$), and C_L can be either unity [64] or calculated by a dynamic method [55].

The dynamic method was first developed by Germano *et al.* (1991) [13], and is originally used to calculate the Smagorinsky coefficient based on an algebraic identity ($\mathcal{L}_{ij} = T_{ij} - \widetilde{\Pi_{ij}}$), where $T_{ij} = \widetilde{\bar{u}_i\bar{u}_j} - \tilde{\bar{u}}_i\tilde{\bar{u}}_j$ represents the subgrid scale stress at test-level filter levels (the test-level filter $\tilde{\bar{\Delta}}$ is typically twice the LES grid $\bar{\Delta}$); and the turbulent stress appearing directly in the LES momentum equation is $\overline{\Pi_{ij}} = \overline{\bar{u}_i\bar{u}_j} - \bar{u}_i\bar{u}_j$. The approach is based on the fact that the Leonard stress tensor, L_{ij}, can be calculated in an actual LES. Using the Smagorinsky method to close both of these two turbulent stresses:

$$\Pi_{ij} - (\delta_{ij}/3)\Pi_{kk} \approx -2C_s\bar{\Delta}^2|\bar{S}|\bar{S}_{ij} \ , \tag{4.5}$$

$$T_{ij} - (\delta_{ij}/3)T_{kk} \approx -2C_s\tilde{\Delta}^2|\tilde{\bar{S}}|\tilde{\bar{S}}_{ij} \ , \tag{4.6}$$

substituting these two equations into the algebraic identity ($\mathcal{L}_{ij} = T_{ij} - \widetilde{\Pi_{ij}}$), and contracting with $\overline{S_{ij}}$ gives:

$$C_s = -\frac{1}{2}\frac{\mathcal{L}_{kl}\bar{S}_{kl}}{\tilde{\bar{\Delta}}^2|\tilde{\bar{S}}|\tilde{\bar{S}}_{mn}\bar{S}_{mn} - \bar{\Delta}^2|\tilde{\bar{S}}|\tilde{\bar{S}}_{mn}\bar{S}_{mn}} \ . \tag{4.7}$$

The dynamic method can also be used to calculate the coefficient C_L in the similarity method [55]. The combination of the similarity method and the dynamic procedure refereed to as the dynamic/similarty method. The dynamic/similarty method has been tested in many studies, and shows relatively good performance in modeling subgrid stress [2, 6, 7, 14, 22, 56, 31, 28, 43, 42]. The subgrid model provided in this work is an extension of the dynamic/similarity method to model the subgrid pressure. The derivation is presented in the next subsection.

4.2 Subgrid model derivation

The derivation of the model proposed here follows similar procedures used in Jaberi and Janes dynamic/similarity model of subgrid reaction rate [20]. Recalling Eq. (1.30):

$$\overline{P(\Psi)} = P(\bar{\Psi}) + P_{sgs}. \tag{4.8}$$

Here, we proposed a similarity closure for this term:

$$P_{sgs} \approx C_1[\widetilde{P(\tilde{\bar{\Psi}})} - P(\tilde{\bar{\Psi}})], \tag{4.9}$$

where $\tilde{\bar{\Psi}}$ represent the grid-level filtering of the resolved variables $\bar{\Psi}$. The grid-level model coefficient, C_1, is calculated by the dynamic procedure similar to the one used

for the subgrid turbulent stresses. In the dynamic procedure, the resolved variables $\bar{\Psi}$ are filtered again with a test-level filter, $\widehat{\Psi}$, which is usually twice the grid-level filter. Applying the test-level filtering on the filtered pressure and resolved primitive variables:

$$\widehat{\overline{P(\Psi)}} = P(\widehat{\bar{\Psi}}) + P_{sgs2}, \tag{4.10}$$

where P_{sgs2} is the test-level subgrid pressure. Using a closure similar to that in Eq. (4.9) for P_{sgs2}:

$$P_{sgs_2} \approx C_2[\widehat{P(\bar{\Psi})} - P(\widehat{\bar{\Psi}})], \tag{4.11}$$

where C_1 is the test-level model coefficient. Using the Germano identity, one can relate the two subgrid pressures as:

$$\begin{aligned} G &= P_{sgs_2} - \widehat{P_{sgs}} \\ &= [\widehat{\overline{P(\Psi)}} - P(\widehat{\bar{\Psi}})] - [\widehat{\overline{P(\Psi)}} - \widehat{P(\bar{\Psi})}] \\ &\approx C_2[\widehat{P(\bar{\Psi})} - P(\widehat{\bar{\Psi}})] - \widehat{C_1}[\widehat{P(\bar{\Psi})} - \widehat{P(\bar{\Psi})}]. \end{aligned} \tag{4.12}$$

Assuming $C_1 = C_2$, $C_1 = \widehat{C_1}$, and minimizing the error in the least-squares sense:

$$\begin{aligned} G &= \widehat{P(\bar{\Psi})} - P(\widehat{\bar{\Psi}}) \\ &\approx C_1[\widehat{P(\bar{\Psi})} - P(\widehat{\bar{\Psi}})], \end{aligned} \tag{4.13}$$

$$\frac{\partial E^2}{\partial C_1} = \frac{\partial [\widehat{P(\bar{\Psi})} - P(\widehat{\bar{\Psi}})] - C_1[\widehat{P(\bar{\Psi})} - P(\widehat{\bar{\Psi}})]^2}{\partial C_1} = 0, \tag{4.14}$$

$$C_1 = \frac{\widehat{P(\bar{\Psi})} - P(\widehat{\bar{\Psi}})}{\widehat{P(\bar{\Psi})} - P(\widehat{\bar{\Psi}})}. \tag{4.15}$$

Finally, the modeled pressure, P_m, is represented in the form:

$$P_m = P(\widetilde{\Psi}) + C_1[\widetilde{P(\bar{\Psi})} - P(\widetilde{\bar{\Psi}})] \ . \tag{4.16}$$

In this work, LES, grid-level, and test-level filter widths of ($3\Delta_1$, $3\Delta_1$, $6\Delta_1$), ($5\Delta_1$, $5\Delta_1$, $10\Delta_1$), and ($12\Delta_1$, $12\Delta_1$, $24\Delta_1$), are examined. In order to calculate the dynamic coefficient, C_1, the DNS data are first filtered at LES filter widths to get $\bar{\Psi}$. Based on $\bar{\Psi}$, the resolved pressure $P(\bar{\Psi})$ is estimated. Then, $P(\bar{\Psi})$ is filtered again by either grid-level filter or test-level filters to get $\widetilde{P(\bar{\Psi})}$ and $\widehat{P(\bar{\Psi})}$, respectively. At the same time, $\bar{\Psi}$ is also filtered again by either grid-level filter or test-levels filter to get $\widetilde{\bar{\Psi}}$ and $\widehat{\bar{\Psi}}$, respectively. Substituting these two values into the Peng-Robinson real gas state equation, $P(\widetilde{\bar{\Psi}})$ and $P(\widehat{\bar{\Psi}})$ are calculated. The last step is filtering $\widetilde{\bar{\Psi}}$ and $P(\widetilde{\bar{\Psi}})$ at test-level filters to calculate $P(\widehat{\widetilde{\bar{\Psi}}})$ and $\widehat{P(\widetilde{\bar{\Psi}})}$, respectively.

4.3 Modeled pressure

The model is tested in both the mixing and the reacting flows. Testing is performed both globally as well as in each conditional regions. The model is tested in Fig. 4.16 by comparing scatter plots of both the modeled (right hand side) and un-modeled pressure vs. the exact filtered pressure. The data correspond to the $Re_0 = 2500$ reacting case, conditioned on each specific localized region. The LES filter width, the grid-level filter width, and the test-level filter width are $8\Delta_1$, $8\Delta_1$, $16\Delta_1$, respectively. In Fig. 4.1, all the filter levels are non-dimensionalized by the initial vorticity thickness $\delta_{\omega 0}$, as $\Delta/\delta_{\omega 0} \approx 1.4$, $\tilde{\Delta}/\delta_{\omega 0} \approx 1.4$, and $\widehat{\Delta}/\delta_{\omega 0} \approx 2.8$, respectively. The right side figures represent the modeled pressure vs. the filtered pressure to some extent, and the left side figures are the resolved pressure vs. the filtered

pressure. Comparing the modeled and un-modeled pressure indicates that the model can improve the pressure due to the reductions in scatter. However, the modeled pressure still overpredicts and underpredicts the filtered pressure, especially in the region related to the large filtered temperature variance [Fig. 4.1(g)]. This again indicates that the temperature variance has a significant correlation to the subgrid scale pressure.

To further compare the modeled pressure with the filtered pressure, we calculate the corresponding correlation coefficients, and present the results in Fig. 4.2, with varying LES filter width [$\Delta/\delta_{\omega 0} = (0, 0.4, 0.9, 1.4)$, $\tilde{\Delta} = \Delta$, $\widehat{\Delta} = 2\Delta$], in each conditional region. For $\Delta/\delta_{\omega 0} = 0$, $\tilde{\Delta} = \widehat{\Delta} = 0$, the DNS field is recovered and all correlations are unity. Figure 4.2(a) presents the coefficients for the $Re_0 = 850$ reacting case, while Fig. 4.2(b) shows the data for the $Re_0 = 2500$ reacting case. These figures show that the modeled pressure is a substantially improved prediction of the filtered pressure compared to neglecting the subgrid pressure. The coefficients increase almost 20% for the two reacting cases, indicating the model significant improves the pressure prediction. In the $Re_0 = 2500$ reacting case, the highest coefficients are found in the regions having large subgrid kinetic energy $\left(\overline{k_{sgs}}/E(\overline{k_{sgs}}) \leq 2\right)$, with the largest filter width $\Delta/\delta_{\omega 0} \approx 1.4$. The reason is explained as follows. The dynamic/similarity model requires the assumption that the most active subgrid scales are those closer to the cutoff and that the scales with which they interact are those immediately above the cutoff wave number [1]. In the region related to the large subgrid kinetic energy, the subgrid scales are more developed, therefore the dynamic/similarity model can improve the pressure prediction more significantly. For the region related to the elevated temperature ($T/T_0 \geq 2$), the coefficient first increases then decreases as the filter width increases. This occurs because the stoichiometric mixture fraction is ≈ 0.15 and, therefore the filter widths include free stream points which have little

subgrid contributions. Finally, the model does show a decreased performance for large Reynolds numbers (Figs. 4.2 and 4.3). Therefore, further examination is warranted.

To further quantify the difference between the modeled pressure and the filtered pressure, the pressure error is defined as $P_{err} = \overline{P(\Psi)} - P_m$. We calculate the PDFs of the ratios of its absolute value to the filtered pressure, with $\Delta/\delta_{\omega 0} \approx 1.4$, $\widetilde{\Delta}/\delta_{\omega 0} \approx 1.4$, and $\widehat{\Delta}/\delta_{\omega 0} \approx 2.8$. The results are presented in Fig. 4.4. The open symbols represent the ratios of subgrid pressure ($P_{sgs} = \overline{P(\Psi)} - P(\bar{\Psi})$) to the filtered pressure, and the filled symbols represent the ratios of $|P_{eer}|/\overline{P(\Psi)}$. The results indicate that the P_{err} is smaller than the subgrid pressure. The corresponding PDFs have a narrower width and the peaks shift to smaller ratios. In the regions having large subgrid mixture fraction dissipation [Fig. 4.4(c)] and large filtered subgid kinetic energy [Fig. 4.4(d)], the model significantly decreases the subgrid pressure error because the majority of the area lies under ratios less than 2%. However, in the regions related to the large filtered temperature variance [Fig. 4.4(e)], the model does not work as well. The PDF curves almost overlap; indicating the similarity closure technique may not be as suitable for the subgrid pressure in these regions.

4.3.1 Modeled pressure gradient

In the LES momentum equation [Eq. (1.7)], the pressure actually appears in its gradient form $[\partial P(\bar{\Psi})/\partial x_i]$. Therefore, although the model developed in this work can decrease the subgrid pressure error, we still need to test its effect on the actual pressure gradient. Figure 4.5 presents the PDFs of the ratios of the magnitude of the modeled pressure gradient to the magnitude of the filtered pressure gradient, for the mixing and the reacting cases, with non-dimensionalized filter levels as $\Delta/\delta_{\omega 0} \approx 1.4$, $\widetilde{\Delta}/\delta_{\omega 0} \approx 1.4$, $\widehat{\Delta}/\delta_{\omega 0} \approx 2.8$. The filled symbols represent the ratio of $|\frac{\partial P_m}{\partial x_i}|/|\frac{\partial \overline{P(\Psi)}}{\partial x_i}|$,

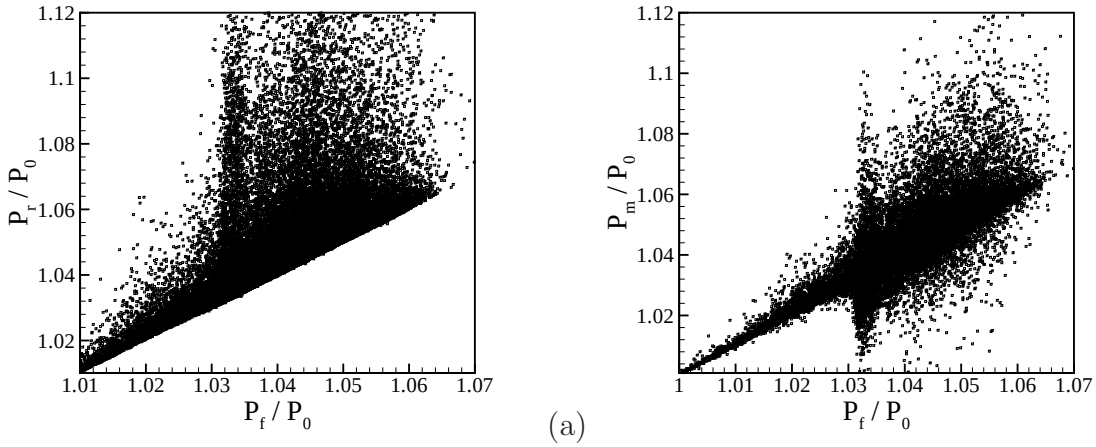
1.12
1.1
1.08
1.06
1.04
1.02
P_r / P_0
1.01 1.02 1.03 1.04 1.05 1.06 1.07
P_f / P_0
1.12
1.1
1.08
1.06
1.04
1.02
P_m / P_0
1 1.01 1.02 1.03 1.04 1.05 1.06 1.07
P_f / P_0

(a)

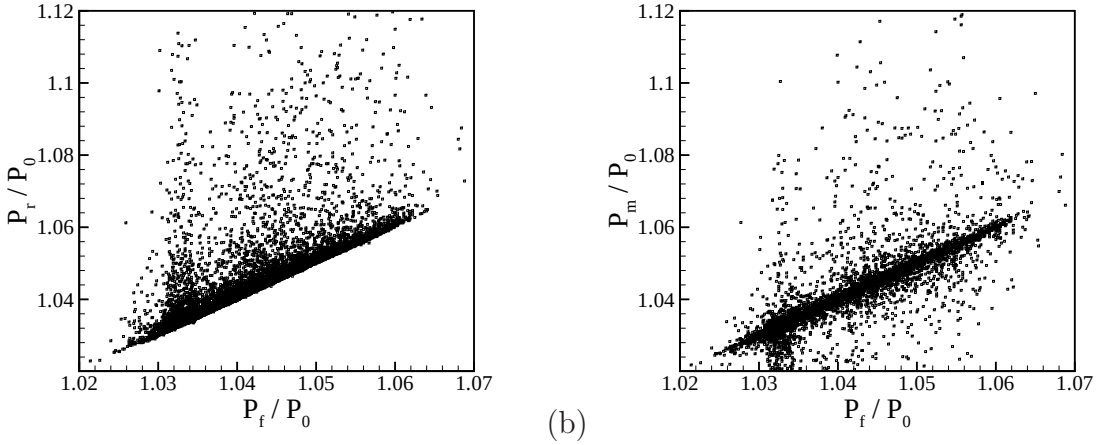
1.12
1.1
1.08
1.06
1.04
P_r / P_0
1.02 1.03 1.04 1.05 1.06 1.07
P_f / P_0
1.12
1.1
1.08
1.06
1.04
P_m / P_0
1.02 1.03 1.04 1.05 1.06 1.07
P_f / P_0

(b)

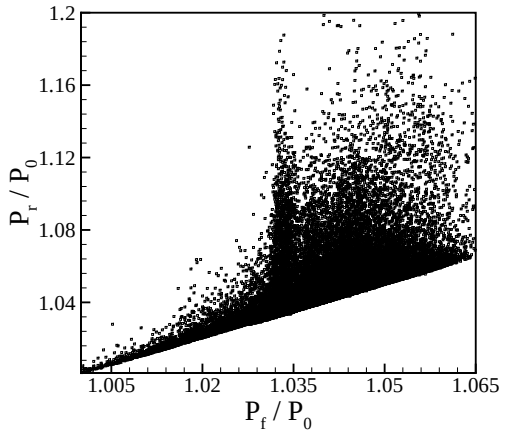
1.2
1.16
1.12
1.08
1.04
P_r / P_0
1.005
1.02
1.035
1.05
1.065
P_f / P_0

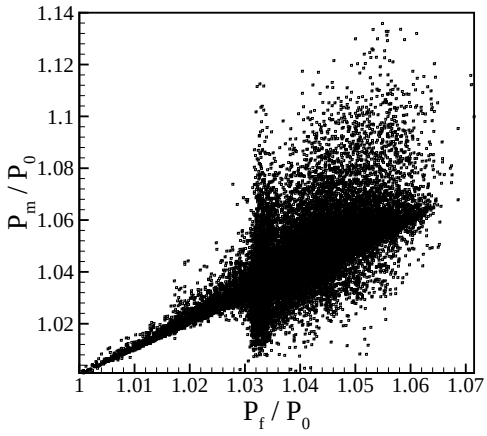
1.14
1.12
1.1
1.08
1.06
1.04
1.02
P_m / P_0
1
1.01
1.02
1.03
1.04
1.05
1.06
1.07
P_f / P_0

(c)

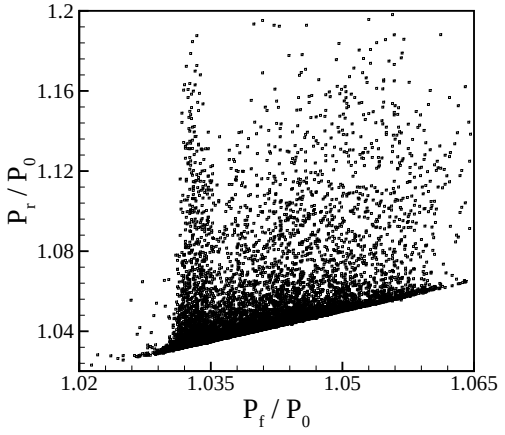
1.2
1.16
1.12
1.08
1.04
P_r / P_0
1.02
1.035
1.05
1.065
P_f / P_0

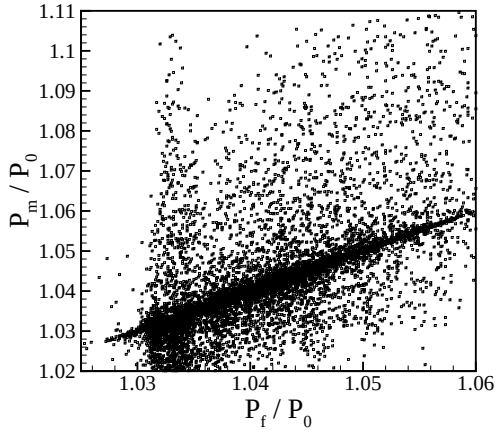
1.11
1.1
1.09
1.08
1.07
1.06
1.05
1.04
1.03
1.02
P_m / P_0
1.03
1.04
1.05
1.06
P_f / P_0

(d)

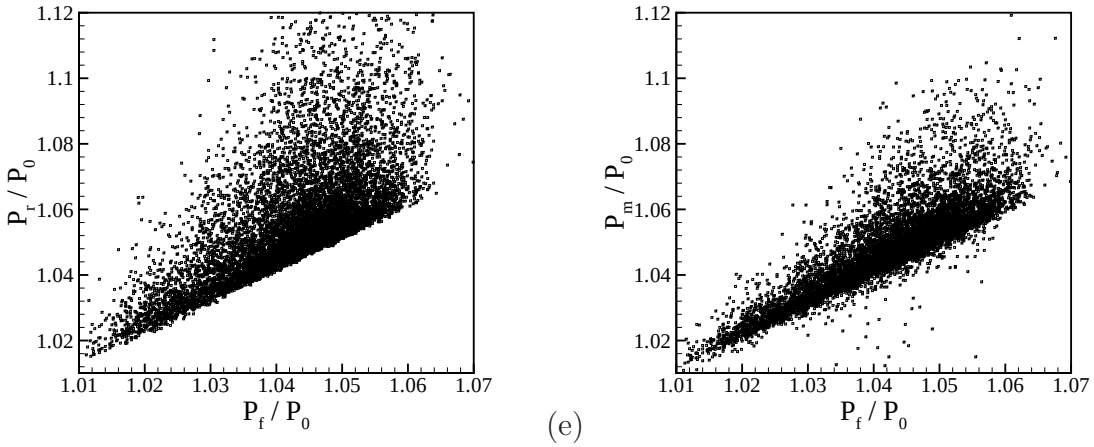
1.12
1.1
1.08
1.06
1.04
1.02
P_r / P_0
1.01 1.02 1.03 1.04 1.05 1.06 1.07
P_f / P_0
1.12
1.1
1.08
1.06
1.04
1.02
P_m / P_0
1.01 1.02 1.03 1.04 1.05 1.06 1.07
P_f / P_0

(e)

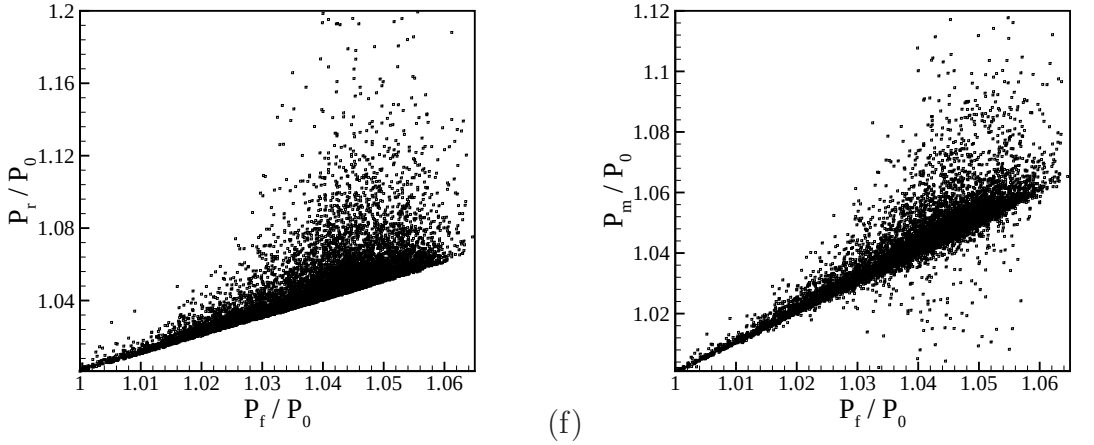
1.2
1.16
1.12
1.08
1.04
P_r / P_0
1 1.01 1.02 1.03 1.04 1.05 1.06
P_f / P_0
1.12
1.1
1.08
1.06
1.04
1.02
P_m / P_0
1 1.01 1.02 1.03 1.04 1.05 1.06
P_f / P_0

(f)

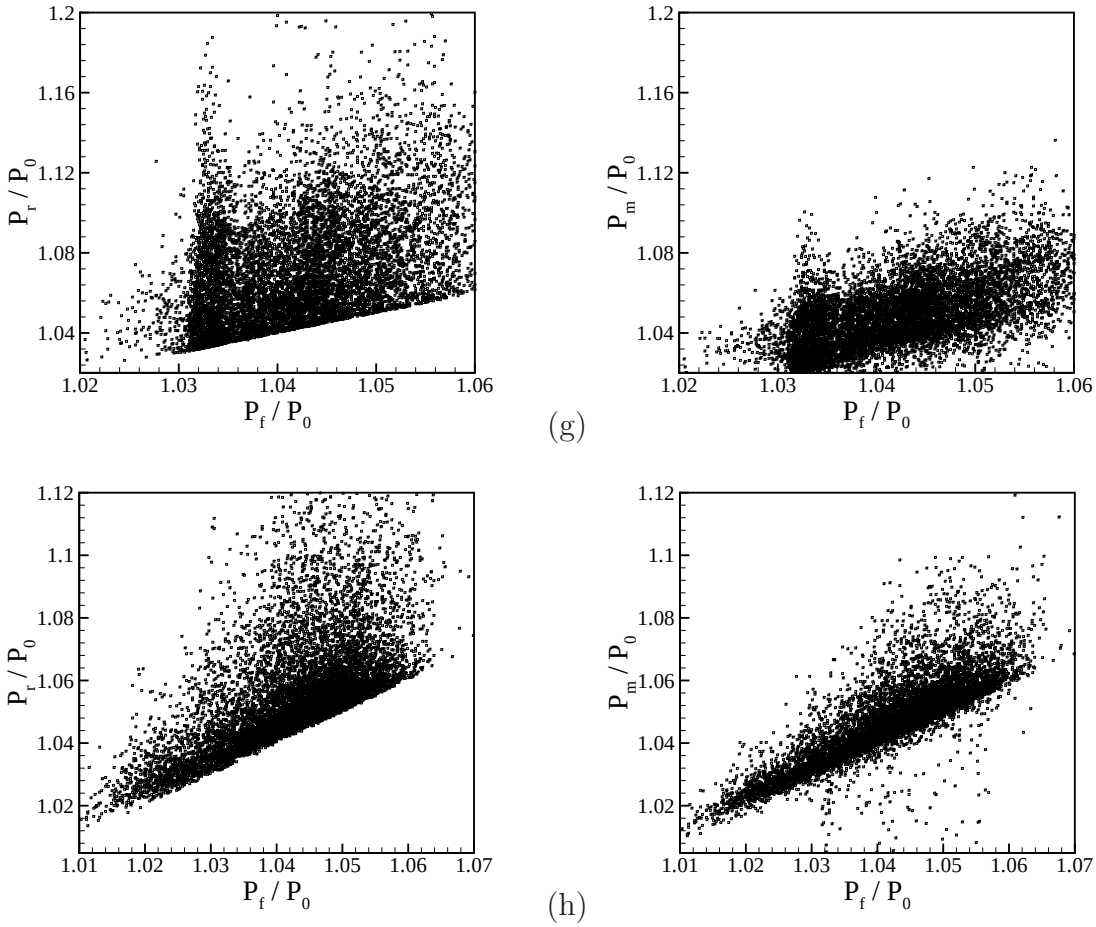

Figure 4.1: Scatter plots of P_m vs. P_f (the right hand side figures), and P_r vs. P_f (left side figures), $\Delta/\delta_{\omega 0} \approx 1.4$, $\widetilde{\Delta}/\delta_{\omega 0} \approx 1.4$, $\widehat{\Delta}/\delta_{\omega 0} \approx 1.4$, conditioned on: (a) $0.01 \leq \phi \leq 0.99$, (b) $0.1 \leq \phi \leq 0.2$, (c) $T/T_0 \geq 2$, (d) $\dot{\omega}^{OH}/E(\dot{\omega}^{OH}) \geq 2$, (e) $\overline{\chi^{\phi}}/E(\overline{\chi^{\phi}}) \geq 2$, (f) $\overline{k_{sgs}}/E(\overline{k_{sgs}}) \geq 2$, (g) $\widetilde{T''^2}/E(\widetilde{T''^2}) \geq 2$, (h) $\widetilde{\phi''^2}/E(\widetilde{\phi''^2}) \geq 2$.

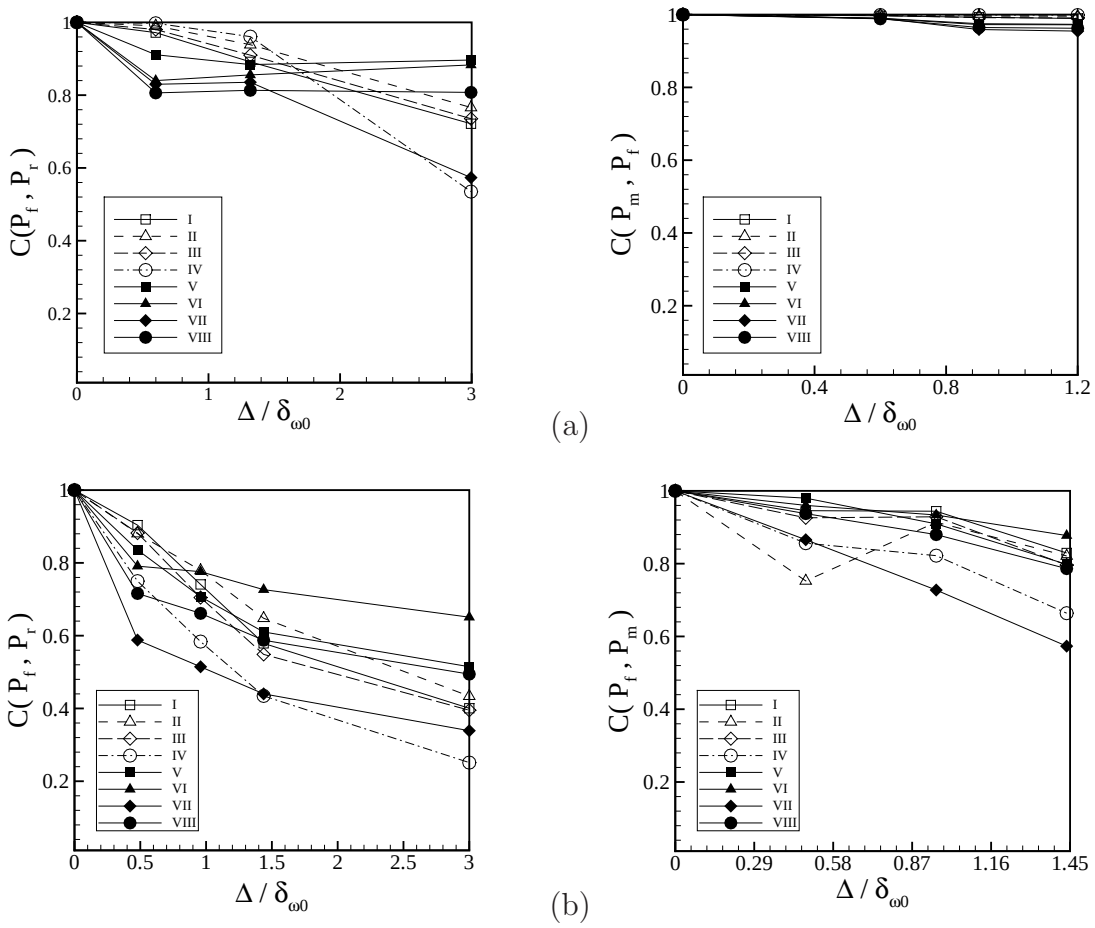

Figure 4.2: Correlation coefficients, C(P_f, P_m) (right side figures) and C(P_f, P_r) (left side figures), as a function of LES filter width, for reacting cases, with (a) $Re_0 = 850$ and (b) $Re_0 = 2500$, conditioned on: (I) $0.01 \leq \phi \leq 0.99$, (II) $0.1 \leq \phi \leq 0.2$, (III) $T/T_0 \geq 2$, (IV) $\dot{\omega}^{OH}/E(\dot{\omega}^{OH}) \geq 2$, (V) $\overline{\chi^{\alpha}}/E(\overline{\chi^{\alpha}}) \geq 2$, (VI) $\overline{k_{sgs}}/E(\overline{k_{sgs}}) \geq 2$, (VII) $\widetilde{T''^2}/E(\widetilde{T''^2}) \geq 2$, (VIII) $\widetilde{\phi''^2}/E(\widetilde{\phi''^2}) \geq 2$.

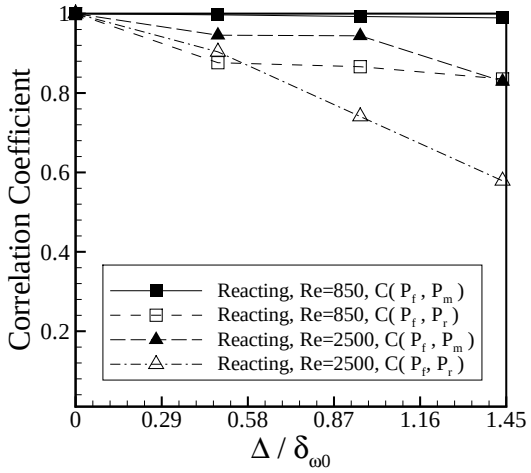

Figure 4.3: Correlation coefficients of P_r and P_m, as a function of Δ, in global region $0.01 \leq \phi \leq 0.99$.

and the open symbols the ratio of $|\frac{\partial P(\bar{\Psi})}{\partial x_i}|/|\frac{\partial \overline{P(\Psi)}}{\partial x_i}|$.

First, the PDFs in the reacting cases are much broader than in the mixing case. Therefore, the subgrid pressure gradient is more important when the chemical reaction is involved. Secondly, the plots indicate the model can improve the pressure gradient somewhat becasue the PDFs of the ratios of $|\frac{\partial P(\bar{\Psi})}{\partial x_i}|$ have narrower widths with higher peaks near the unity. However, unfortunately, the widths are still relatively large. The ratios of $|\frac{\partial P_m}{\partial x_i}|/|\frac{\partial \overline{P(\Psi)}}{\partial x_i}|$ can exceed 5 and be less than 0.5. The modeled pressure gradient still both overpredicts or underpredicts the filtered pressure gradient significantly, and the subgrid pressure gradient error $[\frac{\partial\left(\overline{P(\Psi)}-P_m\right)}{\partial x_i}]$ remains large.

Figure 4.6 presents the PDFs of the ratios of modeled pressure gradient components to the filtered pressure gradient in each flow directions $\left(\frac{\partial P_m}{\partial x_\alpha}/\frac{\partial \overline{P(\Psi)}}{\partial x_\alpha}\right)$. All the regions, except those of large filtered subgrid mixture fraction dissipation rate [Fig. 4.6(e)] and large filtered temperature variance [Fig. 4.6(g)], show that the modeled pressure gradient is closer to the filtered pressure gradient than the resolved

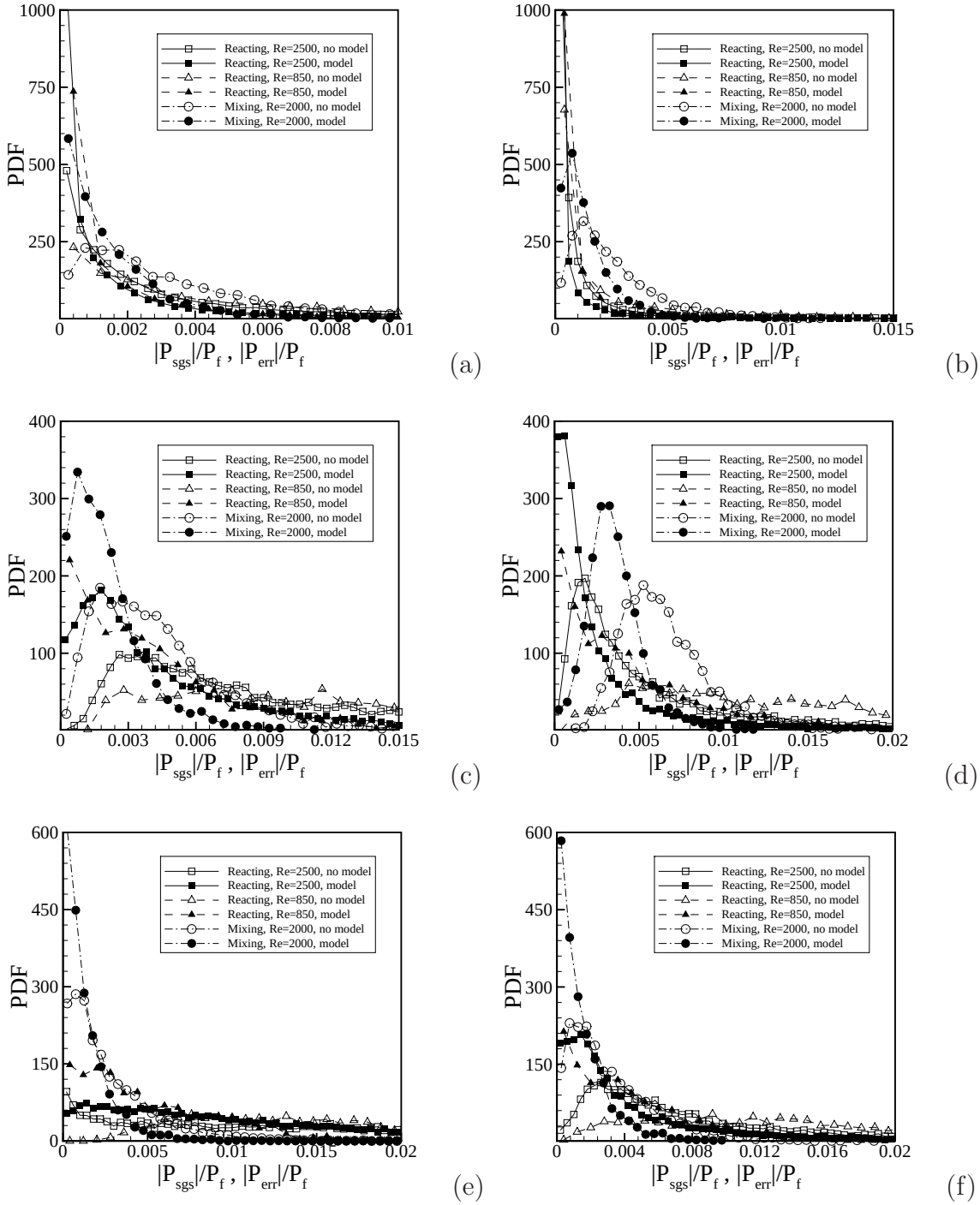

Figure 4.4: PDF of the ratios of $|P_{err}|/P_f$ and $|P_{sgs}|/P_f$, $\Delta/\delta_{\omega 0} \approx 1.4$, $\widetilde{\Delta}/\delta_{\omega 0} \approx 1.4$, $\widehat{\Delta}/\delta_{\omega 0} \approx 2.8$, conditioned on: (a) $0.01 \leq \phi \leq 0.99$, (b) $0.1 \leq \phi \leq 0.2$, (c) $\overline{\chi^{\alpha}}/E(\overline{\chi^{\alpha}}) \geq 2$, (d) $\overline{k_{sgs}}/E(\overline{k_{sgs}}) \geq 2$, (e) $\widetilde{T''^2}/E(\widetilde{T''^2}) \geq 2$, (f) $\widetilde{\phi''^2}/E(\widetilde{\phi''^2}) \geq 2$. The open symbols represent $|P_{sgs}|/P_f$, and the filled symbols represent $|P_{err}|/P_f$.

pressure gradient. Nevertheless, the error remains large. In the regions having large filtered subgrid mixture fraction variance and large filtered temperature variance, the model provides almost no improvement. Again, differentiation amplifies small scale effects; including subgrid scale modeling errors. Therefore, more work is needed to develop a more accurate subgrid model for the subgrid pressure gradient.

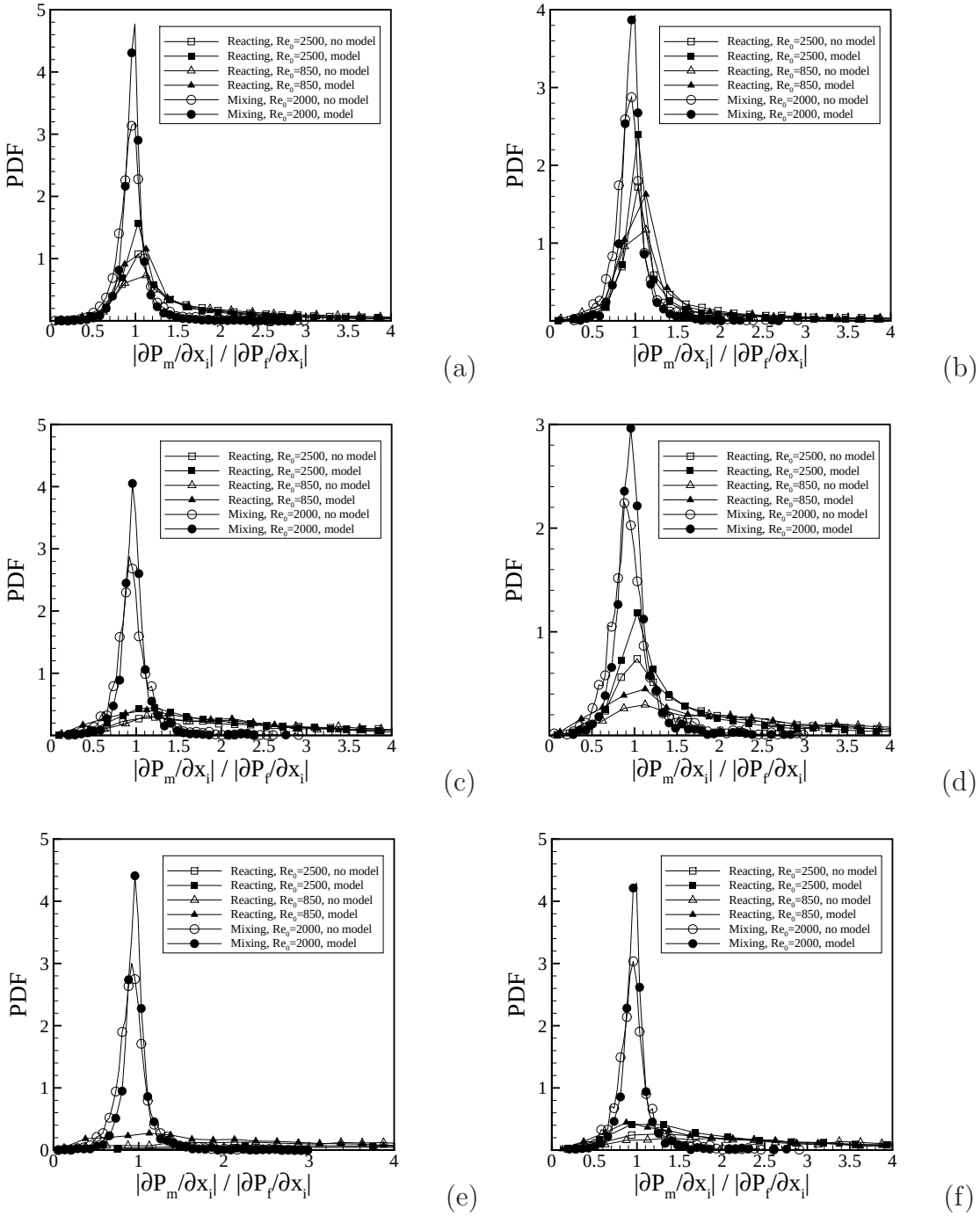

Figure 4.5: PDFs of the ratios of $|\frac{\partial P_m}{\partial x_i}|/|\frac{\partial \overline{P(\Psi)}}{\partial x_i}|$ and $|\frac{\partial P(\bar{\Psi})}{\partial x_i}|/|\frac{\partial \overline{P(\Psi)}}{\partial x_i}|$, $\Delta/\delta_{\omega 0} \approx 1.4$, $\widetilde{\Delta}/\delta_{\omega 0} \approx 1.4$, $\widehat{\Delta}/\delta_{\omega 0} \approx 2.8$, conditioned on: (a) $0.01 \leq \phi \leq 0.99$, (b) $0.1 \leq \phi \leq 0.2$, (c) $\overline{\chi^{\phi}}/E(\overline{\chi^{\phi}}) \geq 2$, (d) $\overline{k_{sgs}}/E(\overline{k_{sgs}}) \geq 2$, (e) $\widetilde{T''^2}/E(\widetilde{T''^2}) \geq 2$, (f) $\widetilde{\phi''^2}/E(\widetilde{\phi''^2}) \geq 2$.

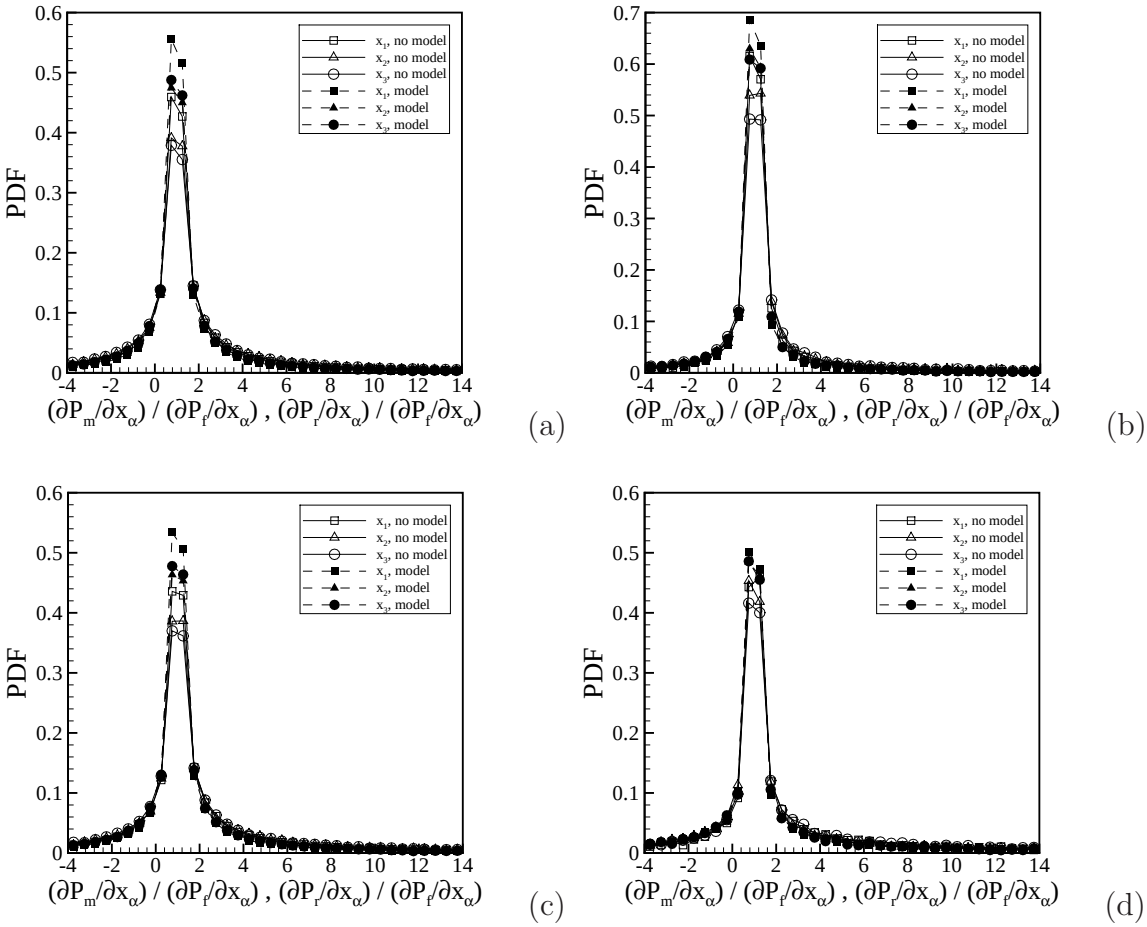
PDF
$(\partial P_m/\partial x_\alpha) / (\partial P_f/\partial x_\alpha)$, $(\partial P_r/\partial x_\alpha) / (\partial P_f/\partial x_\alpha)$
x_1, no model
x_2, no model
x_3, no model
x_1, model
x_2, model
x_3, model
(a)
(b)
(c)
(d)

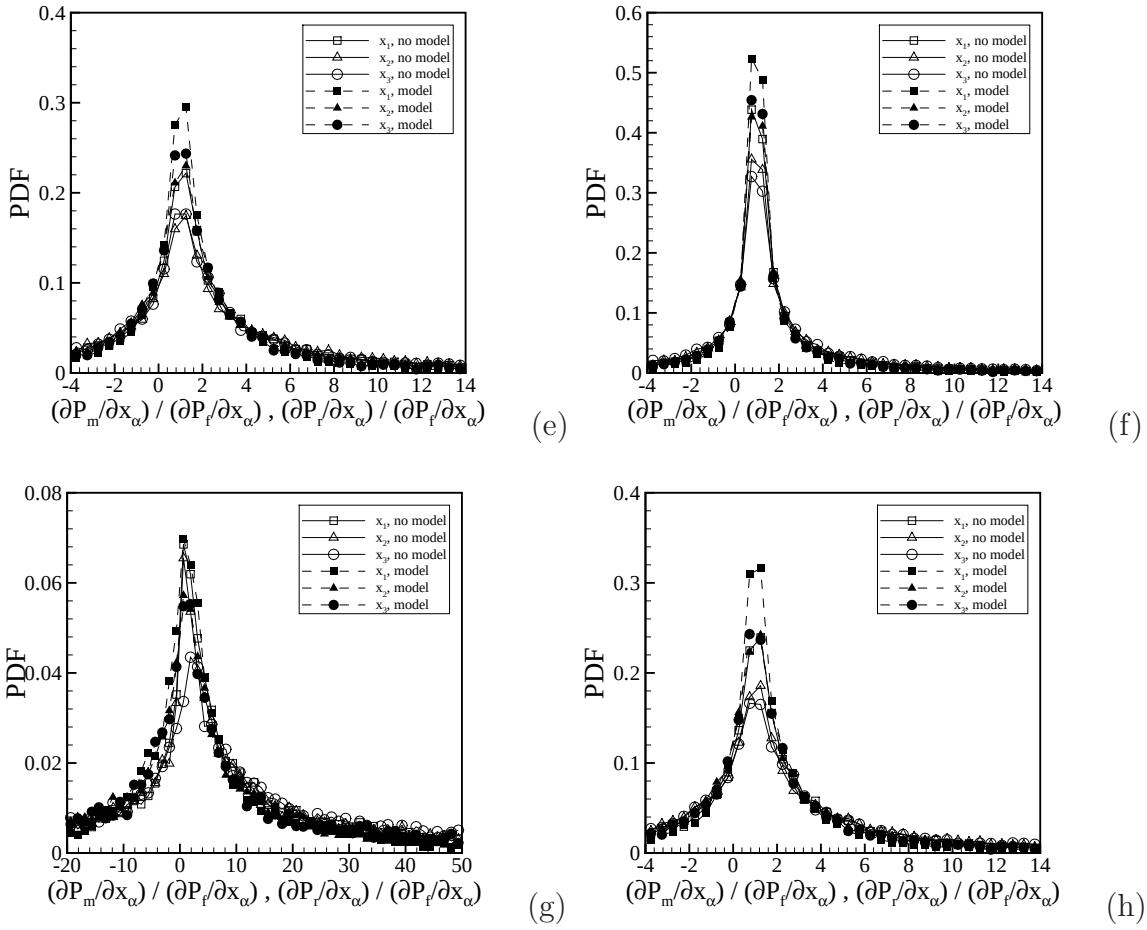

Figure 4.6: PDFs of the ratios of $\frac{\partial P_m}{\partial x_\alpha}/\frac{\partial \overline{P(\Psi)}}{\partial x_\alpha}$ and $\frac{\partial P(\bar{\Psi})}{\partial x_\alpha}/\frac{\partial \overline{P(\Psi)}}{\partial x_\alpha}$, for the $Re_0 = 2500$ reacting flow, $\Delta/\delta_{\omega 0} \approx 1.4$, $\widetilde{\Delta}/\delta_{\omega 0} \approx 1.4$, $\widehat{\Delta}/\delta_{\omega 0} \approx 2.8$, conditioned on: (a) $0.01 \leq \phi \leq 0.99$, (b) $0.1 \leq \phi \leq 0.2$, (c) $T/T_0 \geq 2$, (d) $\dot{\omega}^{OH}/E(\dot{\omega}^{OH}) \geq 2$, (e) $\overline{\chi^\phi}/E(\overline{\chi^\phi}) \geq 2$, (f) $\overline{k_{sgs}}/E(\overline{k_{sgs}}) \geq 2$, (g) $\widetilde{T''^2}/E(\widetilde{T''^2}) \geq 2$, (h) $\widetilde{\phi''^2}/E(\widetilde{\phi''^2}) \geq 2$.

Chapter 5

Conclusions

This work presented an *a priori* analysis of the subgrid pressure in high pressure temporally developing mixing and reacting shear layers based on the DNS data provided by Foster *et al.* [10]. The subgrid pressure is typically neglected by most previous studies without disscusion except for Selle *et al.* [58] who pointed out the potential importance of the subgrid pressure in high pressure binary mixing shear layers. This work extends the study into both high pressure reacting flows as well as into localized regions of the flow field.

The current work provides valuable insight into the subgrid pressure and its gradient relevant to LES. We found that for reacting flows, the chemical reaction causes enhanced scalar gradients and much larger subgrid pressure compared to pure mixing flows. The analyses were conducted both "globally" ($0.01 \leq \phi \leq 0.99$, where ϕ is the mixture fraction) and within locally defined regions of the flame; because turbulent flame dynamic are known to be sensitive to local phenomena. The local regions are defined by conditionally filtering on: the stoichiometric conditions ($0.1 \leq \phi \leq 0.2$), elevated temperature regions ($T/T_0 \geq 2$), high OH reaction rate regions $\left(\dot{\omega}^{OH}/E(\dot{\omega}^{OH}) \geq 2\right)$, where $E(\Psi)$ represents the expected value of Ψ within

$0.01 \leq \phi \leq 0.99$), regions of high filtered scalar dissipation $\left(\overline{\chi^{\phi}}/E(\overline{\chi^{\phi}}) \geq 2\right)$, large subgrid kinetic energy $\left(\overline{k_{sgs}}/E(\overline{k_{sgs}}) \geq 2\right)$, large filtered mixture fraction variance $\left(\overline{\phi''^2}/E(\overline{\phi''^2}) \geq 2\right)$, and large filtered temperature variance $\left(\overline{T''^2}/E(\overline{T''^2}) \geq 2\right)$.

The filtered pressure $\overline{P(\Psi)}$ was compared with the resolved pressure $P(\bar{\Psi})$; noting that the difference between these two terms defines the unclosed subgrid pressure $[P_{sgs} = \overline{P(\Psi)} - P(\bar{\Psi})]$. This study presented scatter plots and correlation coefficients of these two pressures, PDFs of the ratio of the subgrid pressure to the filtered pressure, PDFs of the ratios of the magnitude of the subgrid pressure gradient to the magnitude of the filtered pressure gradient, and the L2 norm of each of the term in the LES momentum equation at varying filter widths.

The analsis of the filtered pressure showed that it can be both overpredicted and underpredicted by the resolved pressure; as large as 13% in the high Reynolds number reacting flows. The difference between these two terms is significant especially in the regions of the large filtered temperature variance, because the Peng-Robinson real gas state equation is highly nonlinear and depends on the temperature. In these regions, the subgrid pressure gradient was also found to be large; indicating the temperature variance is signifcantly correlated to the subgird scale pressure. Both the PDF and L2 norm reveal that the subgrid pressure gradient is of the same order, or even larger than, other terms in LES momentum equation.

Therefore, this work explored a model based on the dynamic/similarity method following the procedure in [20]. The model was derived and tested by evaluating both the modeled pressure, and the modeled pressure gradient. Scatter plots, correlation coefficients, and PDFs of the ratios of the model subgrid pressure to the filtered pressure, suggest the model can significantly improve the pressure itself. However, the improvment is substantially diminished when considering the pressure gradient which appears directly in the LES equations. This occurs because differentiation

amplifies small scale phenomena and, therefore, magnifies pressure modeling errors. This is unfortunately endemic to many LES models. Therefore, future work towards a more accurate model is warranted.

Bibliography

[1] J. Bardina, J.H. Ferziger, and W.C. Reynolds. Improved subgrid-scale models for large-eddy simulation. *AIAA Fluid and Plasma Dyamics Conference*, 1980.

[2] B. Chaouat and R. Schiestel. A new partically integrated transport model for subgrid-scale stresses and dissipation rate for turbulent developing flows. *Phys. Fluids*, 17:17–22, 2005.

[3] S.G. Chumakov. A priori study of subgrid-scale flux of a passive scalar in isotropic homogeneous turbulence. *Physics Rev.*, 78:036313(1)–036313(11), 2008.

[4] P.J. Colucci, F.A. Jaberi, P. Givi, and S.B. Pope. Filtered density function for large eddy simulation of turbulent reacting flows. *Phys. Fluids*, 10:499 – 515, 1998.

[5] A.W. Cook and J.J. Riley. Subgrid-scale modeling for turbulent reacting flows. *Comb. Flame*, 112:593–606, 1998.

[6] S.M. deBruynKops, J.J. Riley, and G. Kosal. Toward large eddy simulations of non-premixed, turbulent reacting flows. *Western States Section of the Combustion Institute Spring Meeting Paper No.97S-051*, 1997.

[7] P.E. DesJardin and S.H. Frankel. Large eddy simulation of a nonpremixed reacting jet: Application and assessment of subgrid-scale combustion models. *Phys. Fluids*, 10:2298–2314, 1998.

[8] G. Eggenspieler and S. Menon. Large-eddy simulation of pollutant emission in a DOE-HAT combustor. *J. Propuls. Power*, 20:1076–1085, 2004.

[9] P. Fernando, M.B. Parlange, C. Meneveau, and W.E. Eichinger. A priori field study of the subgrid-scale heat fluxes and dissipation in the atmospheric surface layer. *J. Atmos. Sci.*, 58:2673–2698, 2001.

[10] J. Foster. *A Priori Anlaysis of Subgrid Scalar Phenomena and Mass Diffusion Vectors in Turbulent Hydrogen-Oxygen Flames.* Masters Thesis, Clemson University, Department of Mechanical Engineering, 2009.

[11] J. Foster and R.S. Miller. Fundamentals of high pressure combustion, chapter in high pressure processes in chemical engineering, Edited by Maximillian Lackner. *ProcessEng Engineering GmbH*, pages 53–75, 2010.

[12] J. Foster and R.S. Miller. A priori analysis of subgrid statistics from direct numerical simulations of high pressure hydrogen-oxygen flames: I subgrid mass flux vectors. *7th US National Meeting*, 2011.

[13] M. Germano, U. Piomelli, P. Moin, and W.H. Cabot. A dynamic subgrid-scale eddy viscosity model. *Phys. Fluids*, 3:1760–1765, 1991.

[14] S. Ghosal, T. Lund, P. Moin, and K. Akselvoll. A dynamic localization model for large-eddy simulation of turbulent flows. *J. Fluid Mech.*, 286:229–255, 1995.

[15] P. Givi. Model free simulations of turbulent reacting flows. *Prog. Eng. Comb. Sci.*, 15:1–107, 1989.

[16] K.G. Harstad, R.S. Miller, and J. Bellan. Efficient high pressure state equations. *AIChE J.*, 43(6):1605–1610, 1997.

[17] D. Haworth and K. Jansen. Large-eddy simulation of unstructured deforming meshes: towards reciprocating IC engines. *Comput. Fluids*, 29:493–524, 2000.

[18] S. Candeland G. Herding, R. Synder, P. Scouflaire, C. Rolon, L. Vingert, M. Habiballah, F. Grisch, M. Pealat, P. Bouchardy, D. Stepowski, A. Cessou, and P. Colin. Experimental investigation of shear coaxial cryogenic jet flames. *J. Prop. Power*, 14(5):826–834, 1998.

[19] S. Hohmann and U. Renz. Numerical simulation of fuel sprays at high ambient pressure: the influence of real gas effects and gas solubility on droplet vaporisation. *Heat Mass Trans.*, 46:3017–3028, 2003.

[20] F.A. Jaberi and S. James. A dynamic similarity model for large eddy simulation of turbulent combustion. *Phys. Fluids*, 10(7):1775–1777, 1998.

[21] C. Jimenez, L. Valino, and C. Dopazo. A priori and a posteriori tests of subgrid scale models for scalar transport. *Phys. Fluids*, 13:2433–2436, 2001.

[22] W. Kim and S. Menon. A new dynamic one-equation subgrid-scale model for large eddy simulations. *AIAA, Aerospace Sciences Meeting and Exhibit, 33rd, Reno, NV; UNITED STATES; 9-12 Jan.*, 1995.

[23] W. Kim, S. Menon, and H. Mongia. Large-eddy simulations of a gas turbine combustor flow. *Comb. Sci. Tech.*, 143:25–62, 1999.

[24] H. Kobayashi. Experimental study of high-pressure turbulent premixed flames. *Exp. Thermal Fluid Sci.*, 26:375–387, 2002.

[25] A. Korucu, J. Foster, and R.S. Miller. A priori analysis of subgrid statistics from direct numerical simulations of high pressure hydrogen-oxygen flames: II subgrid heat flux vectors. *7th US National Meeting*, 2011.

[26] W. Ling, J.N. Chung, T.R. Troutt, and C.T. Crowe. Direct numerical simulation of a three-dimensional temporal mixing layer with particle dispersion. *J. Fluid Mech.*, 358:61–85, 1998.

[27] S. Liu, J.C. Hewson, J.H. Chen, and H. Pitsch. Effects of strain rate on high-pressure nonpremixed n-heptane autoignition in counterflow. *Comb. Flame*, 137:320–339, 2004.

[28] S. Liu, J. Katz, and C. Meneveau. Evolution and modelling of subgrid scales during rapid straining of turbulence. *J. Fluid Mech.*, 387:281–320, 1999.

[29] Y. Liu, N. Tsuboi, H. Sato, F. Higasino, and A.K. Hayashi. Direct numerical simulation on hydrogen fuel jetting from high pressure tank. *Proceedings of the 20th International Colloquium on the Dynamics of Explosions and Reacting Systems,Montreal*, 2005.

[30] K.D. Mare, W. Jones, and K. Menzies. Large-eddy simulations of a model gas turbine combustor. *Comb. Flame*, 137:278–294, 2004.

[31] M. Martin, U. Piomelli, and G.V. Candler. Subgrid-scale models for compressible large-eddy simulations. *Theoretical and Computational Fluid Dynamics*, 13:361–376, 2000.

[32] W. Mayer, A. Schik, and M. Schaffler. Injection and mixing processes in high-pressure liquid oxygen/gaseous hydrogen rocket combustors. *J. Prop. Power*, 16(5):823–828, 2000.

[33] R.S. Miller. Long time mass fraction statistics in stationary compressible isotropic turbulence at supercritical pressure. *Phys. Fluids*, 12(8):2020–2032, 2000.

[34] R.S. Miller, C.K. Madnia, and P. Givi. Structure of a turbulent reacting mixing layer. *Comb. Sci. Tech.*, 99:1–36, 1994.

[35] P. Moin. Advances in large eddy simulation methodology for complex flows. *Int. J. Heat Fluid Flow*, 23:710–720, 2002.

[36] P. Moin and K. Mahesh. Direct numerical simulation: A tool in turbulence research. *Ann. Rev. Fluid Mech.*, 30:539–578, 1998.

[37] C.J. Montgomery, G. Kosaly, and J.J. Riley. Direct numerical simulation of turbulent nonpremixed combustion with multistep hydrogen oxygen kinetics. *Comb. Flame*, 109:113–144, 1997.

[38] A. Mura, V. Robin, and M. Champion. Modeling of scalar dissipation in partially premixed turbulent flames. *Comb. Flame*, 149:217–224, 2007.

[39] S. Palle, C. Nolan, and R.S. Miller. On molecular transport effects in real gas laminar diffusion flames at large pressure. *Phys. Fluids*, 17:103601–1 – 103601–19, 2005.

[40] N. Peters. Laminar diffusion flamelet models in non-premixed turbulent combustion. *Prog. Eng. Comb. Sci.*, 10:319–339, 1984.

[41] N. Peters. *Turbulent Combustion*. Cambridge University Press, 2000.

[42] U. Piomelli. High Reynolds number calculations using the dynamic subgrid-scale stress model. *Phys. Fluids*, 5:1484–1490, 1993.

[43] U. Piomelli and J. Liu. Large eddy simulation of rotating channel flows using a localized dynamic model. *Phys. Fluids*, 286:299, 1995.

[44] H. Pitsch. Improved pollutant predictions in large-eddy simulations of turbulent non-premixed combustion by considering scalar dissipation rate fluctuations. *Proceed. Comb. Institute*, 29:1971–1978, 2002.

[45] H. Pitsch. Large-eddy simulation of turbulent combustion. *Annu. Rev. Fluid Mech.*, 38:453–482, 2006.

[46] H. Pitsch, M.C. Chong, and S. Fedotov. Flamelet modelling of non-premixed turbulent combustion with local extinction and re-ignition. *Comb. Theory Modelling*, 7:317–332, 2003.

[47] S.B. Pope. The probability approach to modelling of turbulent reacting flows. *Comb. Flame*, 27:299–312, 1976.

[48] S.B. Pope. A Monte Carlo method for the PDF equations of turbulent reactive flow. *Comb. Sci. Tech.*, 25:159–174, 1981.

[49] S.B. Pope. Computations of turbulent combustion: Progress and challenges. In *Proceedings of the 23rd Symposium (International) on Combustion*, pages 591–612. Twenty-Third symposium (International) on Combustion, 1990.

[50] V. Raman and H. Pitsch. Large-eddy simulations of a bluff-body stabilized non-premixed flame using a recursive-refinement procedure. *Comb. Flame*, 142:329–347, 2005.

[51] V. Raman and H. Pitsch. A consistent les/filtered-density function formulation for the simulation of turbulent flames with detailed chemistry. *Proceed. Comb. Institute*, 31:1711–1719, 2007.

[52] S. Rao and C.J. Rutland. A flamelet time scale model for non-premixed combustion including chemical kinetic effects. *Comb. Flame*, 133:189–191, 2003.

[53] J.J. Riley, R.W. Metcalfe, and S.A. Orszag. Direct numerical simulations of chemical reacting mixing layers. *Phys. Fluids*, 29(2):406–422, 1986.

[54] M.M. Rogers and M.M. Moser. Direct simulation of a self-similar turbulent mixing layer. *Phys. Fluids*, 6(2):903–923, 1994.

[55] M.V. Salvetti and S. Benerjee. A priori tests of a new dynamic subgrid-scale model for finite-difference large-eddy simulations. *Phys. Fluids*, 7:2831–2841, 1995.

[56] A. Scotti, C. Meneveau, and M. Fatic. Dynamic Smagorinsky model on anisotropic grids. *Phys. Fluids*, 9:1856–1868, 1997.

[57] L. Selle, G. Lartigue, T. Poinsot, R. Koch, and K. Schildmacher. Compressible large eddy simulation of turbulent combustion in complex geometry on unstructured meshes. *Comb. Flame*, 137:489–505, 2004.

[58] L.C. Selle, N.A. Okong'O, J. Bellan, and K.G. Harstad. Modelling of subgrid-scale phenomena in supercritical transitional mixing layers:an a priori study. *J. Fluid Mech.*, 593:57–91, 2007.

[59] C.H. Sohn and S.H. Chung. Effect of pressure on the extinction, acoustic pressure response, and NO formation in diluted hydrogen-air diffusion flames. *Comb. Flame*, 121:288–300, 2000.

[60] Y. Sommerer, D. Galley, T. Poinsot, S. Ducruix, F. Lacas, and D. Veynante. Large eddy simulation and experimental study of flashback and blow-off in a lean partially premixed swirled burner. *J. Turb.*, 5:037, 2004.

[61] C. Stone and S. Menon. Open-loop control of combustion instabilities in a model gas turbine combustor. *J. Turb.*, 4:020, 2003.

[62] L. Vervisch and T. Poinsot. Direct numerical simulation of non-premixed turbulent flames. *Annu. Rev. Fluid Mech.*, 30:655–691, 1998.

[63] B. Vreman, B. Geurts, and H. Kuerten. A priori tests of large eddy simulation of the compressible plane mixing layer. *Journal of Engineering Mathematics*, 29:299–327, 1995.

[64] T.A. Zang, R.B. Dahlburg, and J.P. Dahlburg. Direct and large-eddy simulations of three-dimensional compressible navier-stokes turbulence. *Phys. Fluids*, 4:127–140, 1992.